



الجمهورية الجزائرية الديمقراطية الشعبية

RÉPUBLIQUE ALGÉRIENNE DÉMOCRATIQUE ET POPULAIRE



وزارة التعليم العالي والبحث العلمي

MINISTÈRE DE L'ENSEIGNEMENT SUPÉRIEUR ET DE LA
RECHERCHE

Université Saad Dahleb de Blida

Institut d'Aéronautique et des Études Spatiales

Mémoire présenté en vue de l'obtention du Diplôme de Master

Domaine : aéronautique

Spécialité : avionique

Intitulé :

**Dual-polarimetric weather RADAR
application of spectral polarimetry**

Préparé par :

- FERRAH LISA
- BEN MOKHTAR IMANE

Jury d'évaluation :

- Promoteur : Dr. TIKHEMIRINE
- Président du jury : Mr. LAGHA
- Examineur : Mr. ZABOUT

Année universitaire

2021- 2022

Acknowledgement:

All praises to Allah and His blessing for the completion of this thesis.

First and foremost, I would like to sincerely thank my supervisor Dr. TIKHEMIRINE Mohamed for his guidance, understanding, and patience and most importantly, he has provided positive encouragement and a warm spirit to finish this thesis. It has been a great pleasure and honour to have him as my supervisor.

We wish to extend our special thanks to the jury members, for their interest in our research by agreeing to review our work. In particular: Mr LAGHA Mohand, for doing us the honor of presiding over the jury. As well as Mr ZABOUT Amar, for agreeing to be the examiner of this work.

With the expression of my gratitude, I dedicate this work:

To my family that gave me a dignified education, her love that made me what I am today.

Especially to my father, who has always been by my side to support and encourage me.

For my mother, the source of softness, patience and generosity.

To you my sisters: ***Saliha, Ghenima***, and to my little brother ***Abdenour***.

In memory of my dear grandmother.

Imane

With the expression of my gratitude, I dedicate this work:

To my dear family, who had always supported and encouraged me

To my dear parents, the source of tenderness and love.

To my dear aunts ***Anissa, Lila*** and my grandmother ***Nouara*** for their support and encouragement.

To my brothers ***Arezki*** and ***Nabil***, may God illuminate for them the path of success in their studies.

Specifically, to my uncle ***GRIM MOHAMMED SAID*** and his wife ***OUJJOUDI FARIZA***, the source of ambition, inspiration and self-confidence.

To my friends from Avionics classmate ***Abderrahim*** and ***Kamel***.

LISA

Abstract:

Size sorting of hydrometeors in a precipitation system is a natural phenomenon that shows an increase of terminal velocity of fall with diameter and with microphysical properties of drops. Depending on different sizes, on the microphysical properties and on the dynamical type of a given precipitation system, trajectories of hydrometeors are different. We use dual-pol radar to detect the signature of this phenomenon and help to estimate the precipitation rate in a given and inaccessible location. We will study the fundamentals of the dual-pol weather radar through the parameter equations that can be estimated, the microphysical properties of hydrometeors (size, shape, canting angle, Drop Size Distribution, terminal velocity), simulation of polarimetric variables and application of spectral polarimetry to a hailstorm.

Résumé:

Le tri par taille des hydrométéores dans un système de précipitation est un phénomène naturel qui montre une augmentation de la vitesse terminale de chute en fonction du diamètre et des propriétés microphysiques des gouttes. Selon les différentes tailles, les propriétés microphysiques et le type dynamique du système de précipitation donné, les trajectoires des hydrométéores sont différentes. Nous utilisons un radar bipolaire pour détecter la signature de ce phénomène et aider à estimer le taux de précipitation dans un endroit donné et inaccessible. On étudiera les fondamentaux du radar météorologique polarimétrique à travers les équations de paramètres pouvant être estimés, les propriétés microphysiques des hydrométéores (taille, forme, angle d'inclinaison, distribution de la taille des gouttes, vitesse terminale,...), la simulation des variables polarimétriques et l'application de la polarimétrie spectrale à un orage de grêle.

ملخص:

يعتبر الفرز الحجمي للأجواء المائية في نظام هطول الأمطار ظاهرة طبيعية تظهر زيادة في السرعة النهائية للسقوط مع القطر والخصائص الفيزيائية الدقيقة للقطرات. اعتمادًا على الأحجام المختلفة، وعلى الخصائص الفيزيائية الدقيقة والنوع الديناميكي لنظام ترسيب معين، تختلف مسارات الأرصاد الجوية المائية. نحن نستخدم رادارًا ثنائي القطب لاكتشاف توقيع هذه الظاهرة والمساعدة في تقدير معدل هطول الأمطار في موقع معين يتعذر الوصول إليه. سوف ندرس أساسيات رادار الطقس ثنائي القطب من خلال معادلات المعلمات التي يمكن تقديرها، والخصائص الفيزيائية الدقيقة للأجواء المائية (الحجم، والشكل، وزاوية النوء، وتوزيع حجم الإسقاط، والسرعة النهائية)، ومحاكاة المتغيرات القطبية وتطبيق الطيف. قياس الاستقطاب لعاصفة برد.

Symbols Index

f : Frequency.

c : Speed of light.

λ : Electromagnetic wavelength.

\vec{E} : The electric field vector.

\vec{H} : The magnetic field vector.

r : Range to scatterer.

ω : Angular frequency.

θ, ϕ : Radar beam elevation and azimuth angles

τ : Pulse width.

T_s : Pulse-repetition time (PRT).

T_R : Time delay.

ω_d : Doppler angular frequency.

f_d : Doppler frequency.

v : Radial velocity.

v_a : The maximum unambiguous velocity.

P_t : Peak transmitted power.

P_r : The received power by the radar.

S_{min} : The minimum detectable signal

G : Antenna gain.

σ : Radar cross section.

A_e : Effective area.

R_{max} : The maximum radar range.

L : Loss factor.

η : The reflectivity (cross section per unit volume).

V : The volume sampled by Radar

SNR: Signal-to-Noise Ratio.

D : Hydrometeor equivalent diameter.

$V_t(D)$: The terminal velocity.

R : Rainfall rate.

$N(D)$: Drop Size Distribution (DSD).

N_0 : The number density parameter.

Λ : Slope parameter.

μ : Shape parameter.

D_0 : The median volume diameter.

γ : The canting angle.

g : Gravitational constant.

s : The vertical shear.

U : Horizontal velocity of drop.

f_w : The mixing ratio of ice and water.

S_i : Signal power.

\bar{v}_D : The mean radial velocity.

σ_v : The Doppler velocity spectrum width.

N_i : The noise power.

Z_h : Reflectivity factor.

Z_{DR} : Differential reflectivity.

sZ_{DR} : Spectral differential reflectivity

ρ_{HV} : Correlation coefficient.

$s\rho_{HV}$: The spectral co-polar correlation coefficient.

ϕ_{DP} : The differential phase shift.

$s\phi_{HV}$: Spectral differential phase.

M : Number of signal samples.

$R_i(l)$: The autocorrelation function.

$R_{HV}(l)$: The cross-correlation function.

$\hat{R}_i(l)$: The auto-correlation function estimate.

$\hat{R}_{HV}(l)$: The cross-correlation function.

\hat{S}_i : The signal power estimate.

$s\hat{Z}_{DR}$: Spectral differential reflectivity estimates.

\vec{a}_h : Horizontal direction.

\vec{a}_z : Vertical direction.

$V(t)$: The velocity of hydrometeor.

\vec{F}_n : The net force.

\vec{F}_g : The gravity force.

\vec{F}_d : The drag force.

\vec{U} : Horizontal wind speed.

Illustration Index :

Figure I. 1: Vector of electric field and trajectories of its tip for (a) linear polarization, (b) elliptical polarization, (c) right-hand circular polarization, and (d) left-hand circular polarizations;7

Figure I. 2 : An example of radar waveform	8
Figure I. 3 : The Principle of measurement of a polarimetric radar, from NOAA (National Oceanic and Atmospheric Administration)	16
Figure I. 4: Block diagram for a single H or V channel. [6].....	16
Figure I. 5: dependence of Gamma DSD on N_0 and μ for $D_0 = 5mm$	19
Figure I. 6: (a) Geometry of raindrop, (b) Depiction of raindrop canting angle, adapted from Brussaard (1974). F_D is air drag force acting on the drop [5].....	20
Figure I. 7: The dependence of hail DSD on λ and N_0	22

Figure II. 1 : Doppler spectrum and the three spectral moments	24
Figure II. 2: Differential reflectivity (Z_{DR}) for each drop shape.....	26
Figure II. 3 : $\phi D\rho$ due to hydrometeor concentration	28
Figure II. 4: Mean Doppler velocity estimation, pulse pair method, for $SNR = -5dB$, $SNR = 5dB$, $SNR = 20dB$	34
Figure II. 5 : Spectrum width estimation, pulse pair method, for $SNR = -5dB$,.....	35
Figure II. 6: Mean Doppler velocity estimation, pulse pair method, for $\sigma_v = 0.2 m/s$, $\sigma_v = 2m/s$, $\sigma_v = 20 m/s$	35
Figure II. 7 : Spectrum width estimation, pulse pair method, for $\sigma_v = 0.2 m/s$, $\sigma_v = 2m/s$, $\sigma_v = 20 m/s$	35
Figure II. 8 : Mean Doppler velocity estimation, spectral method, for $SNR = -5dB$ in the left $SNR = 5dB$ in the middle, $SNR = 20dB$ in the right	36
Figure II. 9: Spectrum width estimation, spectral method, for $SNR = -5dB$ in the left $SNR = 5dB$ in the middle, $SNR = 20dB$ in the right.....	36
Figure II. 10: Mean Doppler velocity estimation, spectral method, for $\sigma_v = 0.2 m/s$ in the left $\sigma_v = 2m/s$, in the middle $\sigma_v = 20m/s$, in the right.....	36
Figure II. 11: Spectrum width estimation, spectral method, for $\sigma_v = 0.2 m/s$ in the left, $\sigma_v = 2m/s$, in the middle $\sigma_v = 20 m/s$ in the right.....	37
Figure II. 12: Mean Doppler velocity estimation, spectral method, for $M=64$ in the left, $M=256$ in the right.....	37
Figure II. 13: Spectrum width estimation, spectral method, for $M=64$ in the left, $M=256$ in the right.....	37
Figure II. 14: Spectral differential reflectivity estimates sZ_{DR} for $SNR = -5dB$, $SNR = 5dB$, $SNR = 20dB$	38

Figure II. 15: Spectral co-polar correlation coefficient $spHV$ for $SNR = -5dB$, $SNR = 5dB$, $SNR = 20dB$	38
Figure II. 16: Spectral differential reflectivity estimates $sZDR$ for $spHV = 0.8$, $spHV = 0.9$, $spHV = 0.99$	39
Figure II. 17: Spectral co-polar correlation coefficient estimates $spHV$ for.....	39
Figure III. 1: canting angle under shear	43
Figure III. 2 : The reference plots.....	47
Figure III. 3 : Plots for different environment's properties	48
Figure III. 4 : Plots under the first case	49
Figure III. 5 : Plots under the second case	50
Figure III. 6 : Plots under the third case	50
Figure IV. 1: Surface conditions from Mesonet measurements at 19:00 UTC 24 April 2011 over central Oklahoma.....	53
Figure IV. 2: maximum wind speed, wind direction and the horizontal shear (from interpolated Mesonet wind data at 19:00 UTC.)	54
Figure IV. 3 : Norman sounding data with zonal wind U_x , meridional wind U_y and air temperature at 00 UTC on 24 April 2011. (from Mesonet station)	54
Figure IV. 4 : RHI scan (left panel) and PPI scan (right panel)	56
Figure IV. 5 : Azimuth and elevation angle versus pulse number of the OU-PRIME's RHI scan at 18:58:21 UTC. (From Mesonet stations measurements)	56
Figure IV. 6: A flow chart for data processing to generate spectral moments and polarimetric variables.....	57
Figure IV. 7: A flow chart for data processing on spectral polarimetric variables.....	58
Figure IV. 8: Classes HCA.....	58
Figure IV. 9: Reflectivity, differential reflectivity and co-polar correlation coefficient, radial velocity, spectrum width and differential phase (OU-PRIME RHI at 18:58:21 UTC).....	59
Figure IV. 10: Zoom of radial velocity and spectrum width (OU-PRIME RHI at 18:58:21 UTC)	61
Figure IV. 11 : Plots of the spectral reflectivity, differential spectral reflectivity at 49Km, 49.5Km, 50Km and 50.6Km and the simulation results.....	63

Table of Contents

General Introduction:

1	Motivation:.....	1
2	Brief history of weather radar:	2
3	Literature review:.....	3
4	Scope of the thesis:.....	4

Chapter I: Weather radar fundamentals and microphysical properties of hydrometeors

I.1	Introduction:	5
I.2	Weather Radar fundamentals:	5
I.2.1	Electromagnetic waves and Propagation:	5
I.2.2	Radar theory:.....	7
I.2.3	Doppler radar measurements:.....	8
I.2.3.1	The range resolution ΔR :.....	8
I.2.3.2	Range and maximum unambiguous range:	8
I.2.3.3	Doppler Effect and radial velocity:.....	9
I.2.4	Radar equation:	10
I.2.4.1	General radar equation:	10
I.2.4.2	Weather radar equation:	12
I.2.5	Weather signals:.....	13
I.2.5.1	The transmitted signal:.....	13
I.2.5.2	The echo signal:.....	14
I.2.6	Polarimetric Doppler radar:.....	15
I.3	The microphysical properties of precipitation:.....	17
I.3.1	Rain:	17
I.3.1.1	Size, shape and orientation of raindrops:.....	17
I.3.1.2	The terminal velocity:	18
I.3.1.3	Drop size distribution:	18
I.3.1.4	The canting angle of raindrops:.....	19
I.3.2	Hail:	20
I.3.2.1	Size, shape and orientation of hail:	20
I.3.2.2	Terminal velocity of hail:	21
I.3.2.3	Hail drop distribution:	22

I.3.2.4	Canting angle of hail:	22
---------	------------------------------	----

Chapter II: Signal processing: estimation of base data and spectral polarimetric variable

II.1	Introduction:	23
II.2	Base data:.....	23
II.2.1	Spectral moments:.....	23
II.2.2	Polarimetric variables:.....	25
II.2.2.1	Reflectivity Z_h :.....	25
II.2.2.2	Differential reflectivity:.....	25
II.2.2.3	Correlation coefficient at lag zero:.....	26
II.2.2.4	Differential phase shift ϕ_{DP} :	27
II.3	Base Data estimation:.....	28
II.3.1	Estimation of the spectral moments:	29
II.3.1.1	Using the pulse pair estimator (time domain estimator):	29
II.3.1.2	Using spectral processing (frequency domain estimator):	29
II.3.2	Polarimetric variables estimation:	31
II.3.2.1	Reflectivity factor:.....	31
II.3.2.2	Differential reflectivity:.....	31
II.3.2.3	Correlation coefficient:	31
II.3.2.4	Differential phase:	31
II.4	Spectral polarimetric variables:	31
II.5	Estimation of spectral polarimetric variables:.....	32
II.6	Uncertainty of estimation:.....	33
II.6.1	Simulation of the first and second moment:	34
II.6.2	Simulation of spectral of polarimetric variables:	38
	Conclusion:	39

Chapter III: Shear induced size sorting and simulation

III.1	Introduction:	40
III.2	Definition of size sorting:.....	40
III.3	Equation of movement under shear:.....	40
III.4	Canting angle under shear:.....	42
III.5	Doppler spectrum in turbulence environment:.....	43
III.6	Backscattering cross section:.....	44

III.7	Simulation:	45
	Conclusion:	51
Chapter IV: Application of the results on a hailstorm		
IV.1	Introduction:	52
IV.2	C-band radar observations and Application of spectral polarimetry on the 24 April 2011 Oklahoma City Extreme Hailstorm:	52
IV.2.1	Event description:	52
IV.2.2	DATA collection:	53
IV.3	Radar observations of hailstorm:	55
IV.3.1	Radar specification:	55
IV.3.2	OU-PRIME data processing:	56
IV.3.3	Analysis and discussion:	58
IV.4	Application of spectral polarimetry to hailstorm:	62
	Conclusion:	63
Conclusion and recommendations for future works		
	General conclusion.....	64

General Introduction

1 Motivation:

Air transport is highly dependent on weather conditions during all phases of flight: take-off and cruise and landing. According to FAA statistics, weather is the cause of approximately 70 percent of the delays in the National Airspace System (NAS) of the United States. In addition, weather continues to play a significant role in a number of aviation accidents and incidents. While National Transportation Safety Board (NTSB) reports that weather is a primary contributing factor in 23 percent of all aviation accidents. The total weather impact is an estimated national cost of \$3 billion for accident damage and injuries, delays, and unexpected operating costs. Hazards associated with convective weather include thunderstorms with severe turbulence, intense up- and downdrafts, lightning, hail, heavy precipitation, icing, wind shear, microbursts, strong low-level winds, and tornadoes. American Airlines has estimated that 55 percent of turbulence incidents are caused by convective weather. Anticipating these adverse weather conditions can help mitigate these effects. [1] That is why one of the missions of NATIONAL METEOROLOGICAL SERVICES is to provide the best possible meteorological service to the aeronautics industry. To develop accurate forecasts and provide reliable data, these services must begin with the improvement of detection and measuring instruments.

Weather radar called conventional radar, one of the measuring instruments which are very frequently used to determine the position and intensity of precipitation systems and to observe their dynamics by measuring the horizontal reflectivity and radial velocities of precipitation hydrometeors.

A new radar technology has been deployed by certain meteorological centres: dual-polarimetry. It is based on the emission of horizontally and vertically polarized waves. Thus, new observables strongly linked with microphysics, such as the shape and orientation of hydrometeors, and with the kinematics and dynamics of different types of precipitation are available. These new observations could make it possible to clearly distinguish variations in precipitation types, and to allow a better understanding and modelling of meteorological phenomena (e.g. thunderstorms, turbulence and wind) at various scales of time and space.

2 Brief history of weather radar:

The RADAR (RADIO DETECTION AND RANGING) is a measuring instrument emitting and receiving electromagnetic waves in the field of radio frequencies first developed for military uses to detect the presence of ships and aircraft, and to estimate their positions. The soldiers noticed that parasites were present on their radar images, reflecting the presence of precipitation. From the end of World War II, radars were used to understand the interaction between electromagnetic waves (emitted and received) and precipitating systems. Maynard (1945) was one of the first to carry out such work for the detection of thunderstorms, fronts and cyclones. Since then, numerous studies have been carried out to highlight the various advantages of radar for meteorology. As a result, most developed countries have deployed weather radar networks for the detection and estimation of precipitation, such as the United States with the NEXRAD radar network (NEXT-GENERATION RADAR, or WSR-D88 (Weather Surveillance Radar Doppler 1988)) (Klazura and Imy, 1993) or the French radar network ARAMIS (Application Radar À la Météorologie Infra-Synoptique) (Tabary, 2007).

3 Literature review:

Weather radars not only can improve the warnings of severe and hazardous weather, but can also provide important atmospheric information to forecasters and researcher.

Reflectivity, mean radial velocity and spectrum width are the three fundamental radar measurements, which are termed Doppler moments. They have been used in various applications, such as rain rate estimation, tornado detection, clutter filtering and downburst prediction. With the capability of dual polarization, microphysical properties of scatterers, such as type, size and orientation, can be studied with the help of the polarimetric variables such as differential reflectivity Z_{DR} , differential phase ϕ_{DP} , and cross-correlation coefficient ρ_{HV} . Polarimetric variables have been used to improve several radar applications such as rain rate estimation, drop size distribution (DSD) retrieval, severe hailstorm detection and hydrometeor classification (e.g., Ryzhkov and Zrnić 1996; Bringi and Chandrasekar 2001, Doviak and Zrnić, 1993; Liu and Chandrasekar 2000).

Spectral polarimetry has been used in many applications for improving data quality or retrieving microphysical properties of hydrometeors, especially for mixed types). A combined Doppler and polarimetric measurements were proposed for a new dealiasing technique (Unal and Moisseev, 2004) called spectral polarimetric variables which can further provide the linkage between the hydrometeors' microphysics and dynamics. Spectral processing plays an important role to help in advancing our understanding of the atmosphere, developing new technologies, and improving current algorithms.

Spek et al. (2008) discriminated different types of ice inside a radar resolution volume using dual-polarization spectral analysis at 45° elevation angle. Using varying initial parameters of DSD, the separation between different type of hydrometeor was performed in simulation. Wang (2010) explored the spectral analysis in application for tornado detection. The estimate of spectral reflectivity and spectral differential reflectivity from the mixture of rain and melting hail was retrieved using the melting ratio estimator. Yanovsky (2011) developed the polarization method to retrieve the spectra. The relation between spectra with polarimetric variables, turbulence parameters and DSDs was identified. More recently, the quality of spectral polarimetric variables was derived using the perturbation method (Yu et al., 2012).

The focus of this study is to apply spectral polarimetry induced the size sorting at low elevation angle to detect microphysics, kinematic, and dynamic proprieties of hailstorm.

4 *Scope of the thesis:*

After a brief introduction, the chapter 1 introduces the essential properties of radio waves needed to understand radar principles and describes the effect that the atmosphere has on the path of the radar pulse and its echo. Then, the basic principle of radar operation is explained with a block diagram of dual-polarimetric radar. Additionally, the microphysical properties of hail and rain are provided, which can help understanding the behavior of hydrometeors.

In chapter 2, definition of base data including polarimetric variables and the three spectral moments, and spectral polarimetric variables are presented. Then, the two methods used to derive them are explained in detail. Moreover, a simulation is applied to show the limitations of these methods, and to derive the factors that affect the estimation quality.

The chapter 3 focuses on important microphysical process called "size sorting", specifically, the hydrometeor velocity in vertical shear is derived, and followed by a simulation which is applied to show the signatures of this process on spectral polarimetric variables (in this study, only spectral reflectivity and differential reflectivity are simulated) and mixture of rain and hail in a shear and turbulent environment is considered. The purpose of this simulation is to interpret these signatures to better estimate the microphysical, kinematic, and dynamic properties for a given type of precipitation, and deduce the relationships between them, then exploit the results in the next chapter.

In chapter 4, Radar data collected by the C-band Polarimetric Radar for Innovations in Meteorology and Engineering (OU-PRIME) during a hailstorm event on 24 April 2011 are analyzed, then Spectral polarimetry applied data at 0° elevation angle is capitalized to study the hailstorm's properties in the core using the results gotten in the precedent chapter.

In conclusion, this work is summarized, and future works are suggested.

**Chapter I: Weather radar
fundamentals and
microphysical properties of
hydrometeors**

I.1 Introduction:

To understand the remote sensing of weather by radar, it is necessary to know some basic properties of electromagnetic waves and the effects of the atmosphere on these waves when they propagate between radar and hydrometeors. This chapter reviews the fundamental concepts of waves and presents elementary theories that describe the propagation of waves, and the principles of weather radar. In addition, microphysical properties of different types of hydrometeors are presented briefly.

I.2 Weather Radar fundamentals:

I.2.1 Electromagnetic waves and Propagation:

Coupled fields of electric and magnetic force propagating in space at the speed of light and interact with matter along their paths are called electromagnetic (EM) waves. A packet of these waves has sinusoidal spatial and temporal variation of the electric and magnetic fields. The distance or time between successive wave peaks of the electric (magnetic) force defines the wavelength λ or wave period T (i.e. the reciprocal of the frequency f in hertz). These two important electromagnetic field parameters are related to the speed of light c . [2]

$$c = \lambda f = 3 \times 10^8 \text{ m. s}^{-1}$$

Where:

f : Frequency (s^{-1} or Hz)

c : Speed of light (ms^{-1})

λ : Wavelength (m)

Although a time-harmonic wave can be simply represented by a sinusoidal function or by a complex quantity:

$$z(x, t) = A \cos \left[\omega t + \left(\psi_0 - \frac{\omega x}{v} \right) \right] = \text{Re} [z(x) e^{j\omega t}] \quad (1. 1)$$

The complex quantity $z(x)$ is called a phasor because it is a complex quantity with phase information, but omits the time dependence term. The advantage of introducing the phasor in the complex representation is the convenience it allows in mathematical manipulation. [4]

The electric field wave has time t and range r dependence generally given by:

$$E(r, \theta, \phi, t) = \frac{A(\theta, \phi)}{r} \cos[2\pi f \left(t - \frac{r}{c} \right) + \psi] \text{ (V m}^{-1}\text{)} \quad (1. 2)$$

Where A depends on θ, ϕ (the direction of r from the radiation source), and ψ is usually an unknown but constant transmitter phase angle. [2]

The electric and magnetic fields vectors \vec{E} , \vec{H} are perpendicular to each other and lie in the plane of polarization. Polarization refers to the orientation of the electric field in the polarization plane. The electric field vector of a plane electromagnetic wave traveling in the r direction can be expressed in complex notation as a sum of horizontally and vertically polarized components \vec{E}_h and \vec{E}_v . [3]

The magnitude and direction of \vec{E} will be known if the magnitude and phase angle of horizontal and vertical components of \vec{E} are known (E_h, ψ_h, E_v, ψ_v). If the phase angle difference, between \vec{E}_h and \vec{E}_v , is zero or an integer multiple of π , the wave is said to be linearly polarized. If \vec{E} has only a horizontal component, the wave is said to be horizontally polarized. If \vec{E} lies totally in the vertical plane, the wave is said to be vertically polarized. If both horizontal and vertical components of the wave are simultaneously present, the wave is, in general, elliptically polarized. If the phase angle difference is $\pi/2$, and the amplitudes A_h, A_v of the two components are equal, the wave is right-hand circularly polarized if the phase angle difference is $-\pi/2$, it is left-hand circularly polarized and the electric vector rotates in the counterclockwise direction when viewed in the direction of propagation. [2]

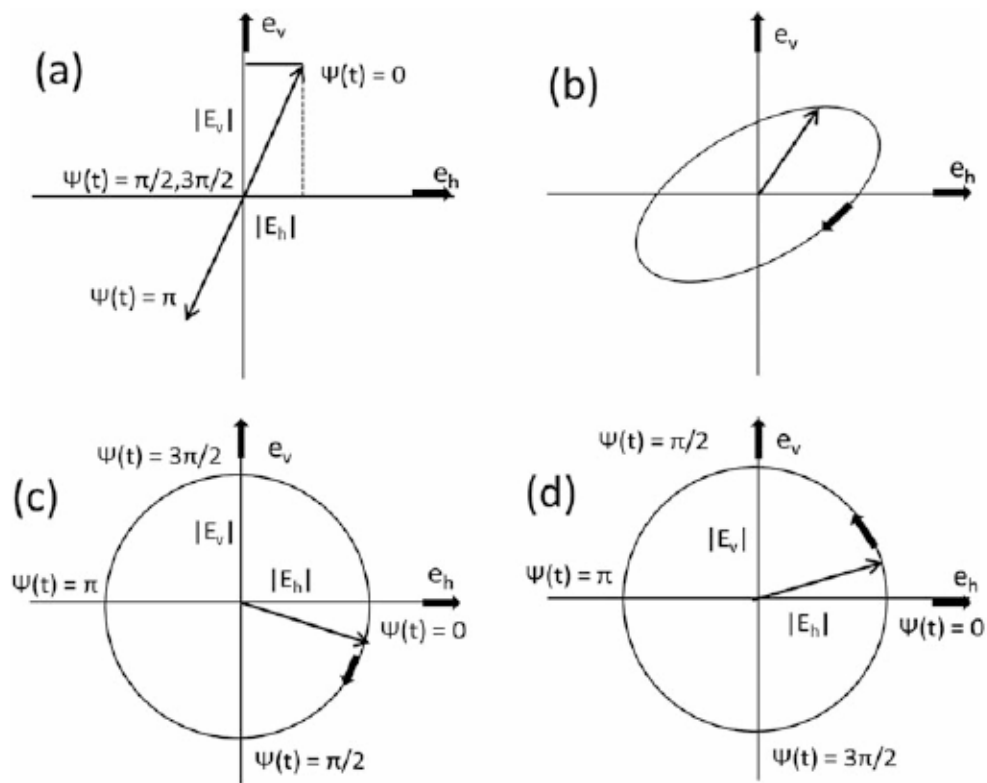


Figure I. 1: Vector of electric field and trajectories of its tip for (a) linear polarization, (b) elliptical polarization, (c) right-hand circular polarization, and (d) left-hand circular polarizations;

I.2.2 Radar theory:

Radar is an electromagnetic system for the detection and location of objects. It operates by transmitting a particular type of waveform, a pulse-modulated sine wave for example, and detects the nature of the echo signal. An elementary form of radar consists of a transmitting antenna emitting electromagnetic radiation generated by an oscillator, a receiving antenna, a receiver (an energy-detecting device). A portion of the transmitted signal is intercepted by a reflecting object (target) and is reradiated in all directions. The receiving antenna collects the returned energy and delivers it to a receiver, where it is processed to detect the presence of the target and to extract its location and relative velocity.

Radars may be classified in several ways due to the criteria of the classification, e.g. receiving and transmitting type, purpose of the use, operating frequency band, signal emitting type (pulse-CW), polarization type. It is also possible to make sub-classifications under the main classification of radars.

So major types of radars have been denominated as monostatic, bistatic, pulse, continuous (CW), Doppler, non-Doppler, weather radar, air surveillance radar, mobile radar, stationary radar, X-Band, L-Band, C-Band, S-Band, K-Band, single polarization radars, polarimetric radars, etc. Although, our main concern is polarimetric Doppler weather radar that will be studied in detail.

I.2.3 Doppler radar measurements:

Doppler radar can determine the component of the velocity of targets toward or away from the radar by measuring the change in frequency of the return signal. This component is called the "radial velocity".

Doppler weather radars typically transmit microwave radiation in bursts of short duration τ (e.g. 10^{-6} seconds or $1 \mu s$). These radars are called Pulsed-Doppler radars to distinguish them from those that emit continuous waves.

It sends out a sequence of modulated pulses as shown in figure, where: τ is the pulse width and T_s is the pulse-repetition time (PRT).

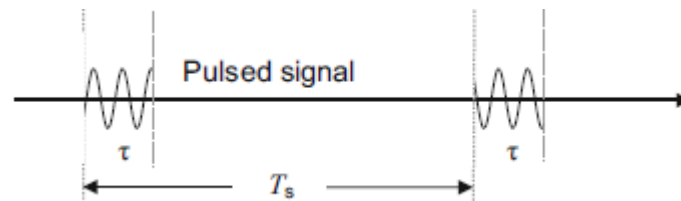


Figure I. 2 : An example of radar waveform

I.2.3.1 The range resolution ΔR :

Defined as the minimum range separation between two targets to be recognized, as following:

$$\Delta R = \frac{c\tau}{2} \quad (1.3)$$

I.2.3.2 Range and maximum unambiguous range:

The range is the distance between radar and target, is determined by the time delay T_R , the signal needs to travel to and back from the target at the light speed c . It is determined by the following equation:

$$R = \frac{cT_R}{2} \quad (1.4)$$

The maximum unambiguous range R_{un} is the range of the target that can be determined from the pulse-repetition time T_s (before the next pulse is transmitted).

$$R_{un} = \frac{cT_s}{2} \quad (1.5)$$

Note the maximum unambiguous range R_{un} does not limit the range of target that radar can measure. However, if a target is located further than R_{un} , the range aliasing occurs.

I.2.3.3 Doppler Effect and radial velocity:

The Doppler Effect or Doppler shift is the change in the frequency of the wave whenever there is a relative motion between the radar and the target. The observed changes in frequency associated with Doppler Effect can be explained as follows:

- As the target moves toward the radar, every successive wave is sent from a position closer to the radar than the previous wave. The time between the arrival of successive wave peaks to the radar is reduced (thus reducing the wavelength), causing an increase in the frequency, as the velocity is constant.
- As the target is moving away from the radar, each wave is emitted from a position further away from the radar than the previous wave, making the waves more spread increasing the wave length and reducing the frequency.

If the target is in motion, R and the phase ψ are continually changing. A change of the phase from a target located at range R is represented in the following equation [4]:

$$\psi = -2\pi \times \frac{2R}{\lambda} \quad (1.6)$$

the doppler angular frequency ω_d is given by:

$$\omega_d = \frac{d\psi}{dt} = -\frac{4\pi}{\lambda} \frac{dR}{dt} = -\frac{4\pi v}{\lambda} = -2\pi f_d \quad (1.7)$$

Where:

f_d : Doppler frequency (Hz)

v : Radial velocity (ms^{-1})

In other words, the Doppler frequency (f_d) is related to the radial velocity (v) by the following formula:

$$v = -\frac{\lambda f_d}{2} \quad (1.8)$$

In weather radar, positive radial velocity indicates the target is moving away from the radar. Similar to maximum unambiguity range, the maximum unambiguous velocity (v_a) is defined as following:

$$v_a = -\frac{\lambda}{4T_s} \quad (1.9)$$

According to equations (1.5) and (1.9) increasing T_s will increase R_{un} , on the other hand, decreasing T_s will mitigate the possibility of velocity aliasing, but radar is more susceptible to overlaid echoes as the maximum unambiguous range decreased. There is always a conflicting tradeoff between R_{un} and v_a , because their product is fixed for a given wavelength. This is also termed range-velocity ambiguity. The range-velocity ambiguity can be reduced by novel techniques such as phase coding or staggered PRT. [6]

1.2.4 Radar equation:

The radar equation relates the received power from radar to the characteristics of the transmitter, receiver, antenna, target, and environment. It is useful not just as a means for determining the maximum distance from the radar to the target, but it can serve both as a tool for understanding radar operation and as a basis for radar design.

1.2.4.1 General radar equation:

If the power of the radar transmitter is denoted by P_t and if an isotropic antenna is used (one which radiates uniformly in all directions), the power density (watts per unit area) at a distance R from radar is given by:

$$\text{Power density from isotropic antenna} = \frac{P_t}{4\pi R^2} \quad (1.10)$$

Radars employ directive antennas, the power density at the target from an antenna with a transmitting gain G is:

$$\text{Power density from directive antenna} = \frac{P_t G}{4\pi R^2} \quad (1.11)$$

The target intercepts a portion of the incident power and reradiates it in various directions. The measure of the amount of incident power intercepted by the target and reradiated back in the direction of the radar depends on the radar cross section σ (Explained in I.2.4.2)

$$\text{Power density of echo signal to radar} = \frac{P_t G}{4\pi R^2} \frac{\sigma}{4\pi R^2} \quad (\text{I. 12})$$

The radar antenna captures a portion of the echo power. If the effective area of the receiving antenna is denoted A_e the power P_r received by the radar is:

$$P_r = \frac{P_t G}{4\pi R^2} \frac{\sigma}{4\pi R^2} A_e \quad (\text{I. 13})$$

Where: $A_e = \frac{G\lambda^2}{4\pi}$

The fundamental form of the radar equation is:

$$P_r = \frac{P_t G^2 \lambda^2 \sigma}{(4\pi)^3 R^4} \quad (\text{I. 14})$$

The maximum radar range R_{max} is the distance beyond which the target cannot be detected. It occurs when the received echo signal power P_r just equals the minimum detectable signal S_{min} :

$$R_{max} = \left[\frac{P_t G^2 \lambda^2 \sigma}{(4\pi)^3 S_{min}} \right]^{1/4} \quad (\text{I. 15})$$

All the parameters are to some extent under the control of the radar designer, except for the target cross section. The radar equation states that if long ranges are desired, the transmitted power must be large, the radiated energy must be concentrated into a narrow beam (high transmitting antenna gain), the received echo energy must be collected by an antenna with high gain, and the receiver must be sensitive to weak signals.

One of the important factors omitted from the simple radar equation was the losses that occur throughout the radar system. The losses reduce the signal-to-noise ratio at the receiver output. The radar equation becomes:

$$P_r = \frac{P_t G^2 \lambda^2 \sigma}{(4\pi)^3 R^4 L} \quad (\text{I. 16})$$

Where L is the same of all loss factor of the radar including: atmospheric loss, receive and transmit line loss, fluctuation loss, etc.

I.2.4.2 Weather radar equation:

The radar equation for meteorological targets differs from point target in the calculation of radar cross section σ .

The radar cross section σ is defined by the projected area at the hydrometeor; it describes the amount of radiation that intercepts with hydrometeor. It depends on many factors: shape and size of the target, orientation in relation to the direction of the radiation, etc.

For distributed targets like rainfall the radar cross section may be written by:

$$\sigma = \eta V \quad (I. 17)$$

Where η is the reflectivity and V is the volume sampled by Radar. And the reflectivity η can be written by:

$$\eta = \sum_{i=1}^N \sigma_i \quad (I. 18)$$

Where N is the number of scatterers by unit volume, and σ_i is the backscattering cross section of i^{th} point scatterer.

Lord Rayleigh and Gustav Mie developed scattering theory that considers the relative quantities of scattering, target size and wavelength.

When the wavelength λ is much greater than the size of target ($\lambda > 16D$) where D is the diameter of target, the backscattering cross section is approximated with the Rayleigh formula:

$$\sigma_i = \frac{\pi^5 D_i^6}{\lambda^4} \left| \frac{m^2 - 1}{m^2 + 2} \right|^2 = \frac{\pi^5 D_i^6}{\lambda^4} |K|^2 \quad (I. 19)$$

With m is complex refractive index. Therefore, the Rayleigh scattering cross section is inversing proportional to the fourth power of wavelength.

When the diameter D of target is comparable with the wavelength (the scattering becomes very sensitive to small changes in target size), the backscattering cross section is approximated to the Mie formula:

$$\sigma = \frac{\pi D^2}{4\alpha^2} \left| \sum_{n=1}^{\infty} (2n + 1)(-1)^n (a_n - b_n) \right|^2 \quad (I. 20)$$

Where $\alpha = \frac{\pi D}{\lambda}$ is the radio electric size or normalized radius, a_n and b_n are the scattering amplitude coefficients of order n . The Mie scattering cross section is proportional to the second power of λ .

When λ is much smaller than target size, radar cross section is independent of λ (called optic region).

If the radar beam is filled with scatterers, the sample volume of V is given approximately by:

$$V = \frac{\pi\theta\phi R^2 c \tau}{8} \quad (I. 21)$$

Where θ and ϕ are the azimuth and elevation beamwidths, and τ is the radar pulse width.

Combining (I.16), (I.19) (using Rayleigh approximation), the weather radar equation becomes:

$$P_r = \frac{P_t G^2 \lambda^2}{(4\pi)^3 R^4 L} \frac{\pi\theta\phi R^2 c \tau \pi^5}{8 \lambda^4} |K|^2 \sum_{i=1}^N D_i^6 \quad (I. 22)$$

This expression can be simplified as follow:

$$P_r = \frac{P_t G^2 \pi^3 \theta \phi c \tau}{512 R^2 \lambda^2 L} |K|^2 \sum_{i=1}^N D_i^6 \quad (I. 23)$$

The antenna gain is not uniform over the beamwidth, Probert-jones assumed a Gaussian shape for antenna beam and derived the following equation:

$$P_r = \frac{P_t G^2 \pi^3 \theta \phi c \tau}{512 (2 \ln 2) R^2 \lambda^2 L} |K|^2 \sum_{i=1}^N D_i^6 \quad (I. 24)$$

I.2.5 Weather signals:

I.2.5.1 The transmitted signal:

The pulse modulator generates a train of microwave pulses that are spaced at the pulse repetition time (PRT) T_s interval (the sampling time interval); each pulse has duration τ of about 1 μ s. An idealized transmitted pulse of power density can be represented as $s(r, \theta, \phi)u(t - r/c)$ [1]:

$$\text{Where: } u\left(t - \frac{r}{c}\right) = \begin{cases} 1 & \frac{r}{c} \leq t \leq \frac{r}{c} + \tau \\ 0 & \text{otherwise} \end{cases} \quad (I. 25)$$

And $s(r, \theta, \phi)$ is the incident radiation power density at range r expressed by:

$$s(r, \theta, \phi) = \frac{P_t G}{4\pi r^2} f^2(\theta, \phi) \quad (I. 26)$$

According to Doviak and Zrnić [2] the incident radiation power density is multiplied by the second power of a function $f(\theta, \phi)$ which represents the normalized power gain pattern (i.e. $f(\theta, \phi)=1$ at θ_0, ϕ_0).

I.2.5.2 The echo signal:

After reception and filtering, the echo signal voltage $V(t, r)$ of a single discrete target is as follow:

$$V(t, r) = Ae^{(-j(\frac{4\pi r}{\lambda} - \psi))} u\left(t - \frac{2r}{c}\right) e^{j2\pi f_d t} \quad (I. 27)$$

Where:

$\left[Ae^{(-j(\frac{4\pi r}{\lambda} - \psi))} u\left(t - \frac{2r}{c}\right) \right]$ is the modulating signal , $\left[e^{j2\pi f_d t} \right]$ is difference frequency signal, the detection serve only to shift the carrier frequency without affecting the modulation envelope, mixing the signal serves to bring f_d to zero, and the difference frequency signal $e^{j2\pi f_d t} = 1$, and the echo signal voltage $V(t, r)$ can be written as follow:

$$V(t, r) = I(t, r) + jQ(t, r) \quad (I. 28)$$

Where $I(t, r) = \left[A/\sqrt{2} u\left(t - \frac{2r}{c}\right) \cos\left(\left(\frac{4\pi r}{\lambda} - \psi\right)\right) \right]$ is the inphase component and $Q(t, r) = \left[-A/\sqrt{2} u\left(t - \frac{2r}{c}\right) \sin\left(\left(\frac{4\pi r}{\lambda} - \psi\right)\right) \right]$ is the quadrature component.

The change in signal phase is extremely small during the modulating envelope $U(t - 2r/c)$. Thus, we measure the target phase shift over an echo-to-echo time T_s rather than during a pulse period, as a result, pulse Doppler radar behaves as a phase sampling device. Samples are at $t = \tau_s + (n - 1)T_s$, with τ_s is the time delay between the n th transmitted pulse and its echo (i.e. $\tau_s = \frac{2r}{c}$). Echo phase and amplitude changes are usually examined in sample-time space at the discrete instants. [7]

Meteorological echoes are composite signals from a large number of hydrometeors, each of which can be considered as a point target, The echo voltage sample $V(\tau_s)$ is a composite of discrete echoes from all scatters:

$$V(\tau_s) = \sum_i A_i e^{j\left(\frac{4\pi r_i}{\lambda}\right)} \quad (I. 29)$$

And A_i is a weight related to the radar cross section, and to the characteristics of the radar design (e.g. the radiation patter $f(\theta, \phi)$, the receiver bandwidth b_6).

The echo sample power averaged or the instantaneous echo power for one transmission is proportional to:

$$p(\tau_s) = \sum_{i,k}^N V(\tau_s)V^*(\tau_s) \quad (I. 30)$$

With N_s is the number of scatterers.

Signal-to-Noise Ratio (SNR) of Weather Targets is given by:

$$SNR = \frac{c_0}{r^2} \frac{z^2 l_r}{b_6 \tau} \quad (I. 31)$$

Where c_0 contains radar constants, l_r is the echo power loss due to finite bandwidth receiver, b_6 is the receiver filter bandwidth ($[b_6 \tau]$ is constant), then SNR is proportional to the square of the transmitted pulsewidth. A formal derivation and taking into consideration the design of the weather radar, leads to the following conclusion: the optimum system consists of a matched Gaussian filter and pulse which together yield the desired resolution (i.e. SNR is maximum if the transmitted pulse has Gaussian shape matched to the filter's Gaussian impulse response).

In this work we consider the noise level as constant.

I.2.6 Polarimetric Doppler radar:

Polarimetric radars have the particularity of emitting electromagnetic waves with two polarizations: a horizontal polarization and a vertical polarization, alternately or simultaneously. Unlike conventional radar which transmits in general of horizontally polarized waves, and only the power backscattered horizontally is evaluated. The additional data (which will be explained in detail in the next chapter) obtained by the polarization diversity radar can eliminate several ambiguities and uncertainties associated with the estimates made using only reflectivity or Doppler Effect. The polarimetric quantities allow the estimation of the precipitation rate to be improved in cases of rain precipitation or mixing of rain and hail. They also allow identification of the type of hydrometeors, ground echoes and abnormal propagation, as well as correction of the effects of radar signal attenuation (Zrnić and Ryzhkov 1999; Illingworth 2003). Polarization diversity radar also provides information related to the shape, size and thermodynamic phase of particles encountered on the radar beam path

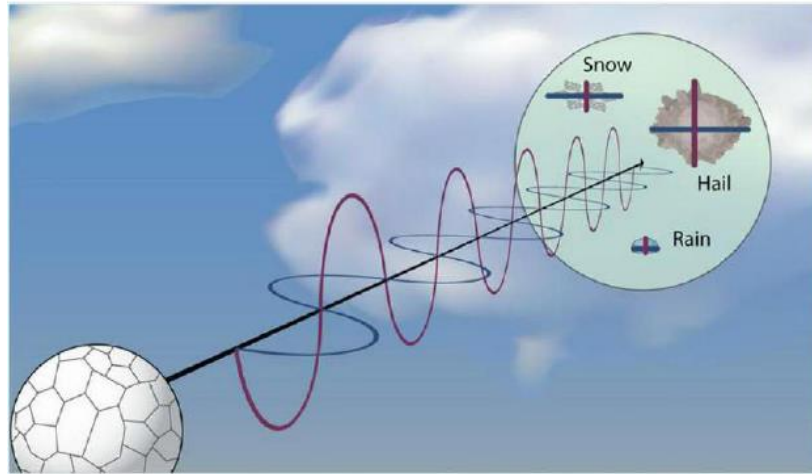


Figure I. 3 : The Principle of measurement of a polarimetric radar, from NOAA (National Oceanic and Atmospheric Administration)

The fundamentals of Polarimetric Doppler radar can be more easily explained by discussing a simplified block diagram of polarimetric homodyne radar (Figure 1.4). Weather radar has an oscillator (the STALO, an acronym for Stabilized Local Oscillator), which generates a very pure continuous microwave (i.e. a spectral line) at a frequency f_t ; this continuous wave is converted to a sequence of microwave pulses by the modulator. Frequency f_t is called the carrier frequency because it carries the modulation pulse. The transmitted microwave pulses, of time duration τ . After receiving the echo signal voltage, it will be treated by different methods which will be presented in the next chapter.

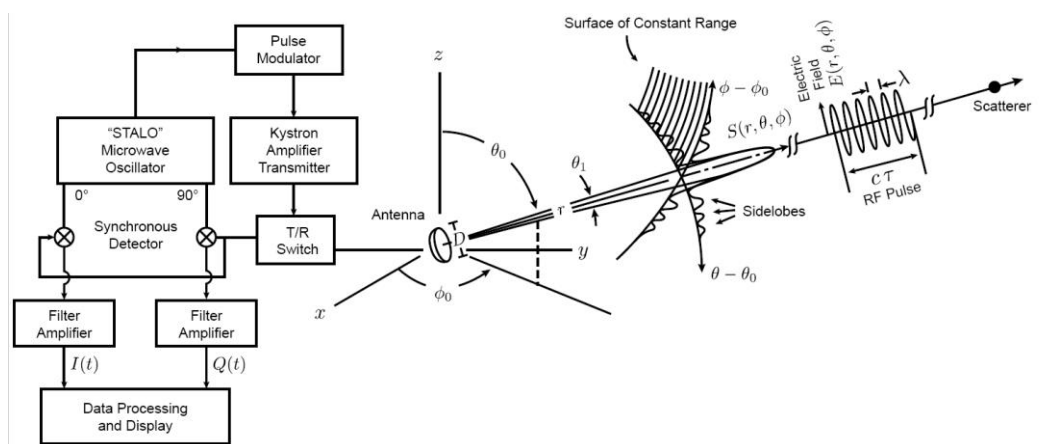


Figure I. 4: Block diagram for a single H or V channel. [6]

I.3 The microphysical properties of precipitation:

Dual-polarization radar can measure parameters that provide microphysical information of precipitation. That will be illustrated herein for each type of hydrometeors.

The microphysical properties of both rain and hail, including shape, terminal velocity and canting angle are discussed.

I.3.1 Rain:

Liquid hydrometeors, and the most common type of precipitation, Rain is droplets of water that have condensed from water vapor in the atmosphere and then precipitated and fall under gravity owing to its weight.

I.3.1.1 Size, shape and orientation of raindrops:

Hydrometeors are usually modeled as oblate or prolate spheroids, and each is characterized by its equivalent volume (or equivolume) diameter $D = (ab^2)^{1/3}$, where 'a' is a symmetry (or rotation) axis of spheroid and 'b' is its transverse axis. For oblate hydrometeors $a < b$, whereas for prolate hydrometeors $a > b$ [3].

The droplets of diameter $D < 0.35$ mm are mainly spherical and the droplets up to 1 mm of diameter have an approximate shape by an oblate spheroid. Larger drops have a progressively flattened base, then concave ($D \sim 4$ mm); larger drops become unstable, so they have a high probability of breaking into smaller drops. [8]

An oblate spheroid has a semi-major axis of a and semi-minor axis of b , its volume V is given by:

$$V = \frac{4\pi}{3} a^2 b = \frac{\pi}{6} D^3 \quad (I. 32)$$

Where D is the equivalent diameter,

The axis ratio (or aspect ratio), that represents the oblateness, which is the shape of a raindrop [4]:

$$\beta = \frac{b}{a}$$

To quantitatively describe the raindrop shape as a function of its equivolume diameter D : [8]

$$\beta = 1.03 - 0.62D \quad (I. 33)$$

I.3.1.2 The terminal velocity:

An accurate knowledge of terminal velocity of precipitation of drops is needed for interpreting Doppler radar data. The terminal velocity is the velocity at which the forces acting on the drop are in balance (i.e. the drag and the gravity forces acting on the drop are equals but opposites in direction). The terminal velocity has been studied experimentally (e.g. Gunn & Kinzer 1949 [9], Beard & Prupacher 1969 [10]). Several equations have been published that describe the terminal velocity of fall as a function of the drop diameter. [11]

The power law relation:

$$V_t(D) = AD^B \quad (I. 34)$$

This relation proposed by Marshall and Palmer 1948, where A and B are constants; is mostly inaccurate. [12]

The fall speed reaches 9.2 m.s⁻¹ for $D > 6$ mm. The Gunn and Kinzer (1949) relation for more accuracy near the ground is: [9]

$$V_t(D) = 9.65 - 10.3e^{-0.6D}$$

Drops fall faster in rarified air, so $V_t(D)$ needs to be adjusted at higher altitudes. Foote and Dutoit (1969) deduce the dependence of the terminal velocity on the air density that can be approximated by: [13]

$$V_t(D, \rho) = V_t(D) \left(\frac{\rho_0}{\rho}\right)^{0.4} \quad (I. 35)$$

Where ρ_0 : is the air density at ground level and ρ is air density at the level of observation. [2]

I.3.1.3 Drop size distribution:

A better understanding of the microphysical processes of precipitation can be obtained by the drop size distribution (DSD). This distribution is expressed as the number of raindrops per unit size interval per unit volume in space. [14]

The first analytical description of the DSD was given by Marshall and Palmer (1948), and their relation is now the most widely used and the simplest. They derived the inverse exponential dependence between the DSD's and the drop diameters parameterized by only one variable, rain rate R . The relation is given as:

$$N(D) = N_0 e^{-\Lambda D} \quad (I. 36)$$

Where:

N_0 ($m^{-3} mm^{-1}$): is the intercept parameter,

Λ (mm^{-1}): is the slope parameter $\Lambda = 4.1R^{-0.21}$, [12]

A more general form of DSD is described by the three-parameter gamma distribution (Ulbrich 1983):

$$N(D) = N_0 D^\mu e^{-\Lambda D} = N_0 D^\mu e^{-\frac{(3.67+\mu)D}{D_0}} \quad (I. 37)$$

Where μ is the dimensionless shape parameter of distribution $-3 \leq \mu \leq 8$, D_0 is the median volume diameter (i.e. is the mean of drops inside a radar resolution volume). [15]

It should be noted that the gamma DSD behaviour is governed by the three parameters N_0 , μ and Λ . The graphs below represent the dependence of the gamma DSD on shape parameter μ (in the left where $N_0 = 8000$, $D_0 = 5mm$), N_0 (in the right where $\mu = 3$, $D_0 = 5mm$):

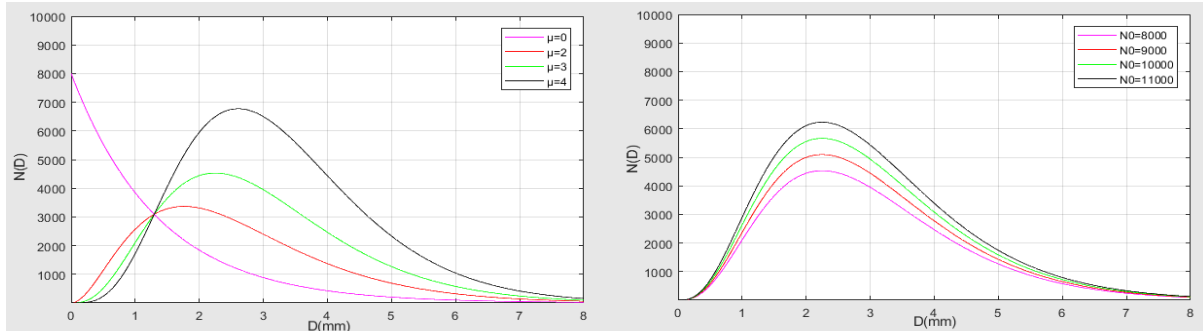


Figure I. 5: dependence of Gamma DSD on N_0 and μ for $D_0 = 5mm$

As shown in the left panel of the Figure I.5, it is obvious that μ makes a little influence on the concentration; so the increase of μ , the mean of DSD shifts marginally to a higher value. On the left of the figure (I.5), the mean of DSD is similar for different N_0 values with slightly larger peak values for large N_0 .

I.3.1.4 The canting angle of raindrops:

The quantitative understanding of the polarization discrimination between precipitations requires more information about the canting angle of raindrops. In the presence of wind shear, raindrops which normally fall with flat bottom parallel to the surface of the earth have been observed to tilt from the horizontal. [16]

The canting angle of raindrops which is the angle between the vertical and the scatterer's axis of symmetry notated γ is given by:

$$\tan\gamma = s \frac{V_t}{g} \quad (I. 38)$$

Where s is the vertical shear, and V_t is the terminal velocity, g is the acceleration of the gravity.

This equation applies for $t \gg \tau = \frac{V_t}{g}$, where s is set at $t=0$.

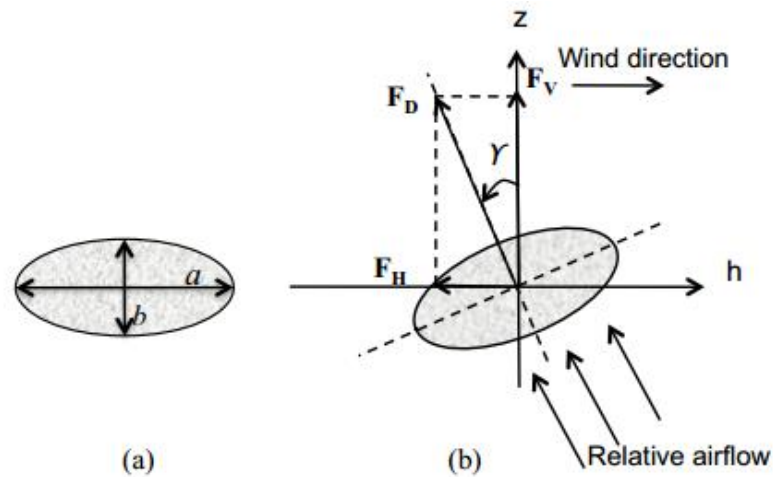


Figure I. 6: (a) Geometry of raindrop, (b) Depiction of raindrop canting angle, adapted from Brussaard (1974). F_D is air drag force acting on the drop [5]

The canting of raindrop from a constant horizontal force:

$$\tan\gamma = \frac{F_H}{F_V} = \frac{\frac{dU}{dt}}{-g} \quad (I. 39)$$

Where:

F_H : Horizontal component of drag force on the drop.

F_V : Vertical component of drag force on drop.

U : Horizontal velocity of drop. [17]

I.3.2 Hail:

Hail is another type solid, frozen form of precipitation, formed principally by the accumulation of ice particles that may reach a very large size.

I.3.2.1 Size, shape and orientation of hail:

Magono and Lee (1966) demonstrated that there are over 60 different types of ice crystals, depending on their size [18]. The diameter of hail varies between 5 to 25 mm. [19]

Hydrometeors are generally modeled as spheroids (Bringi and Chandrasekar 2001) [20]. The relation between the smallest and biggest particle size is given by a power law:

$$w(D) = \xi D^\zeta \quad (I. 40)$$

Where w is the smallest dimension of the hail, and D is the largest dimension and $\xi = 0.8, \zeta = 1$.

The majority of hailstones have axis ratios of 0.8, with melting hail having a lower axis ratio of 0.6–0.8. [4]

Melting hail can have different thicknesses of water coating and is considered as wet hail. It is composed of a mixture of ice and water. The density of ice particles can be modeled, as a function of maximum particle size D : [19]

$$\rho_H = kD^l \quad (I. 41)$$

Where $k = 0.9$ and $l = 0$.

The mass and area projected to the normal flow of the particles need to be parameterized as a function of diameter is given by:

$$m(D) = \alpha D^\beta \quad (I. 42)$$

$$A(D) = \gamma D^\sigma \quad (I. 43)$$

Where: $\alpha = 0.466 \text{ g}$ and $\beta = 3 \text{ g}$, $\gamma = 0.625 \text{ cm}^2$ and $\sigma = 2 \text{ cm}^2$. [22]

The ice water content (IWC) is the amount of ice estimated in a volume unit, defined in g.m^{-3} by:

$$IWC = \int_{D=0}^{\infty} m(D)N(D)dD \quad (I. 44)$$

I.3.2.2 Terminal velocity of hail:

The terminal velocity of hail derived by from Mitchell in 1996 is an equation according to the largest diameter D given by: [21]

$$V_t(D) = \alpha v \left(\frac{2\alpha g}{\rho_a v^2 \gamma} \right)^b D^{b(\beta+2-\sigma)-1} \quad (I. 45)$$

Where the kinematic viscosity of air is v , ρ_a is the density of air and $a, b, \alpha, \beta, \sigma, \gamma$ are constants, (with: $a = 1.86$ and $b = 0.5$).

I.3.2.3 Hail drop distribution:

The gamma distribution and the exponential distribution are commonly used; we choose the two-parameter DSD (i.e. the exponential DSD), which is expressed by the following formula:

$$N(D) = N_0 e^{-\lambda D} = N_0 e^{-3.67 \frac{D}{D_0}} \quad (I. 46)$$

The following plots show the dependence of exponential DSD on slope parameter λ (in the left where $N_0 = 5000$), N_0 (in the right where $\lambda = 0.5$):

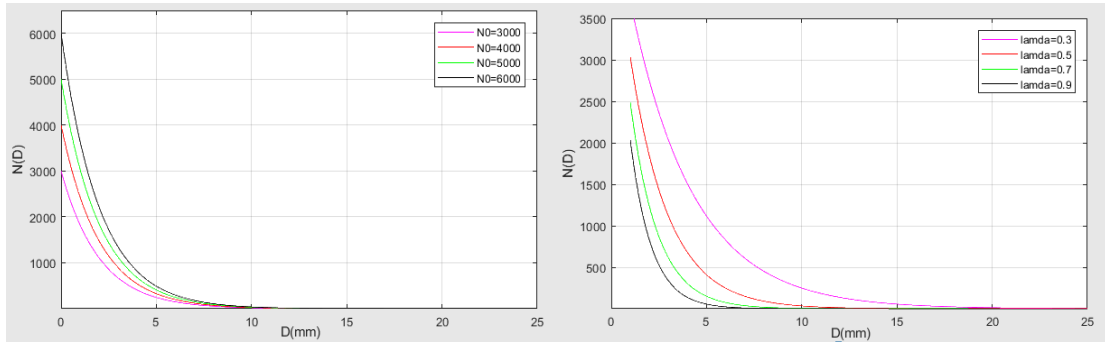


Figure I. 7: The dependence of hail DSD on λ and N_0

In Figure I.7, hail's DSD with different values of N_0 is shown in the left panel. With the exponential distribution, the DSD is dominant by smaller hails; $N(D)$ increases as increasing N_0 . On the right panel, it is evident that a low value of λ provides more large drops than a higher value of λ

I.3.2.4 Canting angle of hail:

Falling hail will be canted because of external forces like wind, turbulence, and shear. Dry hail tumbles while falling and are therefore considered to have random orientations, for wet hail fall with a major horizontal axis the mean canting angle is 0° and the standard deviation SD is about 5° (Aydin and Zhao, 1990) [23] and Vivekanandan et al. (1993) [24] proposed 1° for hail.

The mean canting angle is calculated by the equation (I.38) as the raindrops and the SD is parameterized as a function of the water fraction (ice-water mixtures) $60^\circ(1 - 0.8f_w)$ (Jung et al 2007).

In this work, the first method is applied where the SD of the canting angle is $5^\circ(1 - 0.8f_w)$, with f_w is the mixing ratio of ice and water with value between 0 to 1. [25]

**Chapter II: Signal
processing: estimation of
base data and spectral
polarimetric variable**

II.1 Introduction:

This study is devoted to the estimation and interpretation of polarimetric radar measurements. The present section provides the definition of the spectral moments, the polarimetric variables and their estimations for major interest to meteorological purposes.

II.2 Base data:

Base data of polarimetric weather radar includes: the spectral moments (signal power, mean radial velocity, spectrum width) from each H and V channels, and the polarimetric variables (reflectivity factor, differential reflectivity, Co-polar correlation coefficient, and differential phase).

II.2.1 Spectral moments:

There are three spectral moments:

- Weather signal power or the zeroth moment of the Doppler spectrum, it can be related to liquid water content or precipitation rate in the resolution volume.
- Mean radial velocity or the first moment of the power-normalized spectra, representing the weighted average of all hydrometeor velocities within a radar resolution volume.
- Spectrum width: square root of the second moment of the Doppler spectrum, a measure of velocity dispersion within the resolution volume. It is contributed by a number of sources as shown in the following equation [2]:

$$\sigma_v^2 = \sigma_s^2 + \sigma_a^2 + \sigma_d^2 + \sigma_o^2 + \sigma_t^2 \quad (II. 1)$$

where σ_s^2 is due to shear, σ_a^2 is due to antenna motion, σ_d^2 is due to different fall velocity of hydrometeors, σ_o^2 is due to change of hydrometeor orientation and σ_t^2 is due to turbulence.

The spectral moments are defined from the Doppler spectrum which has a Gaussian shape: [2]

$$S_i(v) = \frac{S_i}{\sqrt{2\pi}} e^{-\frac{v-v}{2\sigma_v^2}} + \frac{N_i}{2v_\alpha} \quad (\text{II. 2})$$

S_i : The signal power (the zeroth moment): it is the area under the Doppler spectrum (i = H or V channels). Its expression is:

$$S_i = P = \int S(f)df = \int S(v)dv \quad (\text{II. 3})$$

\bar{v}_D : The mean radial velocity (the first moment); the first central moment of Doppler spectrum; it represents the weighted average of all hydrometeors velocities in radar resolution volume. Its expression is:

$$\bar{v}_D = \int \frac{vS(v)dv}{S(v)dv} \quad (\text{II. 4})$$

σ_v : The spectrum width (the second moment): is defined as the standard deviation of the Doppler spectrum: it represents the consistency of phase-shift of signals; it is contributed by a number of sources: shear, antenna motion, different fall velocity of hydrometeors, the change of hydrometeor orientation, the turbulence. Its expression is:

$$\sigma_v^2 = \int \frac{(v-\bar{v}_D)^2 S(v)dv}{S(v)dv} \quad (\text{II. 5})$$

v_α : The maximum unambiguous velocity

N_i : The noise power and $\frac{N_i}{2v_\alpha}$ is the noise level (considered as a constant).

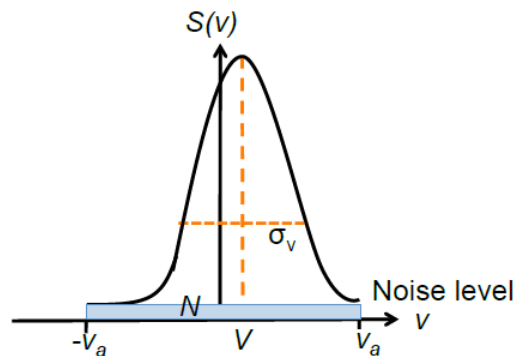


Figure II. 1 : Doppler spectrum and the three spectral moments

II.2.2 Polarimetric variables:

II.2.2.1 Reflectivity Z_h :

Reflectivity is a measure of the amount of wave energy reflected by precipitation or other particulates in atmosphere. Al-Khatib et al. (1979) represented the radar reflectivity η in the following equation: [26]

$$\eta = \int_0^{\infty} \sigma(D)N(D)dD \quad (\text{II. 6})$$

Where $\sigma(D)$ is the expected back-scattering cross section for a hydrometeor of diameter D and $N(D)$ is the DSD is the radar resolution volume.

The reflectivity factor is related to the radar reflectivity; using Rayleigh approximation the backscattering cross section from equation (I.19) the equation (II.6) will be [2] :

$$\eta = \int_0^{\infty} \frac{\pi^5 D^6}{\lambda^4} |K|^2 N(D)dD = \frac{\pi^5 |K|^2}{\lambda^4} \int_0^{\infty} N(D)D^6 dD \quad (\text{II. 7})$$

The integral $\int_0^{\infty} N(D)D^6 dD$ is defined by the reflectivity factor Z . [2]

The equation of radar reflectivity η becomes:

$$\eta = \frac{\pi^5 |K|^2}{\lambda^4} Z \quad (\text{II. 8})$$

As a result, the reflectivity factor can be represented in the following equation:

$$Z = \frac{\lambda^4}{\pi^5 |K|^2} \eta \quad (\text{II. 9})$$

Z is usually expressed in logarithmic scale (dB): $Z \text{ (dB)} = 10 \log (Z)$. This factor is used to indicate the intensity of the storm.

II.2.2.2 Differential reflectivity:

Differential reflectivity is the logarithmic ratio of the reflectivity factors at H and V polarizations in dBZ units. It is the difference between horizontal and vertical reflectivity; its values range from -7.9 to 7.9 decibels. It's expressed by:

$$Z_{DR} = 10 \log \left(\frac{Z_H}{Z_V} \right) \text{ (dB)} \quad (\text{II. 10})$$

For spherical hydrometeors, the reflectivity values for both the horizontal and vertical dimensions of hydrometeors are approximately equal. This leads to a difference of horizontal to vertical reflectivity of approximately 0, which means Z_{DR} is approximately 0dB.

Horizontally oriented hydrometeors such as rain drops will have a positive Z_{DR} , while vertically oriented hydrometeors such as vertically oriented ice crystals will have negative Z_{DR} . [27]

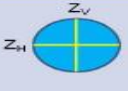
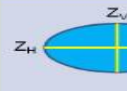
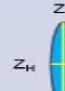
Spherical (drizzle, small hail, etc.)	Horizontally Oriented (rain, melting hail, etc.)	Vertically Oriented (i.e. vertically oriented ice crystals)
		
$Z_H \sim Z_V$	$Z_H > Z_V$	$Z_H < Z_V$
$Z_H - Z_V \sim 0$	$Z_H - Z_V > 0$	$Z_H - Z_V < 0$
$ZDR \sim 0 \text{ dB}$	$ZDR > 0 \text{ dB}$	$ZDR < 0 \text{ dB}$

Figure II. 2: Differential reflectivity (Z_{DR}) for each drop shape

For Rain: Smaller rain drops tend to be spherical, but as the raindrops become larger, they become more oblate, Therefore, rainfall characterized by larger drop sizes have larger value of Z_{DR} .

For Hail: The Z_{DR} of hail varies as a function of hailstone size, shape, and how much liquid water is located on or within the hailstone. If hail tumbles chaotically as it falls, the resulting measured Z_{DR} is close to zero, as the stones appear to be spherical in the statistical sense. Nonzero Z_{DR} values measured in large hail above the environmental 0°C level. When small hail becomes completely water-coated due to melting process, it appears as a giant raindrop to the radar, this leads to very high Z_{DR} values.

For snow and ice crystals, it can take on different sizes and shapes along with varying degrees of particle density, it can lead to different values of Z_{DR} .

II.2.2.3 Correlation coefficient at lag zero:

At lag 0, the correlation coefficient is a measure of how similarly the horizontally and vertically polarized pulses are behaving within a pulse volume. Its values can range from 0.2 to 1. When the pulses behave very similarly result in high ρ_{HV} .

It is arguably the most important dual-pol base product because it allows forecasters the ability to determine if radar echoes are dominated by a homogeneous precipitation type, a mixture of precipitation types, or non-precipitation, (depends on the shape, oscillation, wobbling, and canting angle distribution of hydrometeors). It's expressed by [27]:

$$\rho_{HV} = \frac{|R_{HV}(0)|}{\sqrt{S_H S_V}} \quad (\text{II. 11})$$

Where S_H and S_V are signals power from H and V channels and the cross correlation function at zero lag is defined as:

$$R_{HV}(0) = \frac{1}{M} \sum_0^{M-1} V_V(m) V_H^*(m) \quad (\text{II. 12})$$

Most meteorological echoes tend to have ρ_{HV} values greater than 0.9. Exceptions include giant hail and melting snow flakes, which can dip to as low as 0.70. For non-meteorological echoes, the correlation coefficient is rarely greater than 0.90 except for certain types of static ground clutter which can get as high as 0.99 in some cases.

II.2.2.4 Differential phase shift ϕ_{Dp} :

The difference between the horizontal and vertical phase shifts. The equation is just a simple subtraction; the positive differential phase shift occurs when horizontal phase shift is greater than vertical. it is expressed by:

$$\phi_{Dp} = \text{Arg}[R_{HV}(0)] \quad (\text{II. 13})$$

The shape of the target affects the differential phase shift:

- Horizontally oriented targets will produce an increasing, positive differential phase shift with increasing range.
- Vertically oriented targets will produce a decreasing, negative differential phase shift with increasing range.
- Spherical targets will produce near zero differential phase shifts with increasing range.

Additionally, differential phase shift is dependent on particle concentration. Increasing the number of particles will result in an increase in differential phase shift. For example, the more horizontally oriented targets there are within a pulse volume, the higher the positive differential phase shifting.

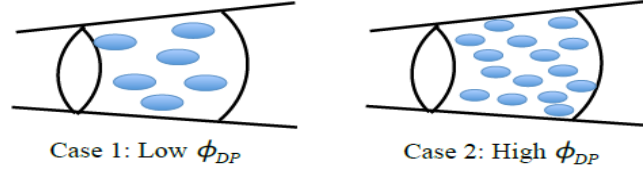


Figure II. 3 : ϕ_{DP} due to hydrometeor concentration

II.3 Base Data estimation:

Assume the receiver signal (voltage) V_i is measured after each transmitted pulse for a total of M measurements (samples) and $V_i(m)$: represent the m^{th} sample include both $I_i(m)$: in-phase component, $Q_i(m)$: the quadrature component:

$$V_i(m) = I_i(m) + jQ_i(m) = a_i(m)e^{-j\phi_i(m)} \quad i: \text{H or V channels (II. 14)}$$

To estimate the base Data, two methods are performed. The pulse pair estimator (covariance estimator) which calculates the moments and the polarimetric variables using the auto-covariance function in time domain and the spectral processing based on discrete Fourier transform DFT of the receiver signal. [2]

The autocorrelation and the cross-correlation functions are defined by the following expressions:

$$R_i(l) = \langle V_i(m)V_i^*(m+l) \rangle \quad (\text{II. 15})$$

$$R_{HV}(l) = \langle V_H^*(m)V_V(m+l) \rangle \quad (\text{II. 16})$$

The discrete Fourier transform DFT of a signal sampled M times is defined as:

$$Z(f) = \sum_{m=0}^{M-1} V_i(mT_s)e^{-j2\pi fT_s m} \quad (\text{II. 17})$$

Where $f = kf_0 = \frac{k}{MT_s}$, according to Doviak and Zrnić 1993, to simplify this equation we can eliminate f_0 , T_s from calculation to obtain a compact form of DFT as following:

$$Z(k) = \sum_{m=0}^{M-1} V_i(m)e^{-j2\pi f \frac{k}{M} m} \quad (\text{II. 18})$$

II.3.1 Estimation of the spectral moments:

II.3.1.1 Using the pulse pair estimator (time domain estimator):

It is based on the auto-correlation function estimate of the received signal, which can be expressed as follows:

$$\hat{R}_i(l) = \frac{1}{M-l} \sum_0^{M-l-1} V_i(m+l)V_i^*(m) \quad i: \text{H or V channels} \quad (\text{II. 19})$$

Where:

l : is the time lag between two time series.

The cross-correlation function estimate is expressed by:

$$\hat{R}_{HV}(l) = \frac{1}{M} \sum_0^{M-1} V_V(m+l)V_H^*(m) \quad (\text{II. 20})$$

The average total power corresponding to the received signal $V_i(m)$ is obtained by averaging M samples of simultaneous power [2] [3]:

$$\hat{P}_i = \frac{1}{M} \sum_{m=0}^{M-1} P_i(m) = \frac{1}{M} \sum_{m=0}^{M-1} |V_i(m)|^2 = \hat{R}_i[0] \quad (\text{II. 21})$$

Where \bar{P} : the averaged total power, M is the number of samples processed. And because the scatters are moving, a noise power will be added, thus the signal power estimated by the follow equation:

$$\hat{S}_i = \hat{P}_i - \hat{N}_i = \frac{1}{M} \sum_{m=0}^{M-1} |V_i(m)|^2 - \hat{N}_i \quad (\text{II. 22})$$

Where: \hat{N}_i is the noise power estimated for horizontal and vertical channel.

The radial velocity is estimated by [2]:

$$\hat{v}_D = \frac{-\lambda}{4T_s} \text{Arg}[\hat{R}_i(1)] \quad (\text{II. 23})$$

The spectrum width is estimated by:

$$\hat{\sigma}_v = \frac{\lambda}{2\sqrt{2}\pi T_s} \left| \ln \left[\frac{\hat{R}_i(0)-N}{\hat{R}_i(1)} \right] \right|^{1/2} \text{sgn} \left[\frac{\hat{R}_i(0)-N}{\hat{R}_i(1)} \right] \quad (\text{II. 24})$$

Where $\hat{R}_i(0)$ and $\hat{R}_i(1)$ is the auto-correlation function for $l = 0$ and $l = 1$.

II.3.1.2 Using spectral processing (frequency domain estimator):

The spectral moments are defined from auto or cross-spectra of horizontal and vertical signals. Given a wide sense stationary (WSS) process $v(t)$, the power spectrum $S(f)$ for each horizontal and vertical channel is defined as the Fourier transform of the autocorrelation function:

$$S_i(f) = \int_{-\infty}^{\infty} R_i(l) e^{-i2\pi fl} dl \quad (\text{II. 25})$$

The power conservation relates the Doppler spectrum $S_i(v)$ to the power spectrum $S_i(f)$ via the follow equation [2]:

$$S_i(v) = \frac{z}{\lambda} S_i(f) \quad (\text{II. 26})$$

When the spectrum or the autocorrelation are known, all pertinent signal parameters can be readily obtained:

Using the equation (II.18) the discrete Fourier transform (DFT) of M radar samples from H and V channels using hamming window $w(m)$ is writing as shown in this formula:

$$Z_i(k) = \sum_{m=0}^{M-1} w(m) V_i(m) e^{-j2\pi \frac{k}{M} m} \quad (\text{II. 27})$$

Where $k = 0, 1, \dots, M-1$, the spectrum w is the weighting window (the window is used to reduce the side lobes of spectra).

The Doppler spectrum is estimated using the periodogram as shown in the following equation:

$$\hat{S}_i(k) = \frac{1}{M} |z_i(k)|^2 = \frac{1}{M} \left| \sum_{m=0}^{M-1} w(m) V_i(m) e^{-j2\pi \frac{k}{M} m} \right|^2 \quad (\text{II. 28})$$

The mean velocity estimate is:

$$\hat{v}_{Di} = -\frac{\lambda}{2MT_s} \left[k_m + \frac{1}{\hat{P}_i} \sum_{k=-\frac{M}{2}}^{k_m + \frac{M}{2}} (k - k_m) \hat{S}_i[\text{mod}_M(k)] \right] \quad (\text{II. 29})$$

Where \hat{P} : is the total power in the peroidogram, $\text{mod}_M(k)$: is the remainder of the division of k by M, this equation is found by Doviak and Zrnić, 1993 to avoid biases aliasing of symmetric spectrum.

The spectrum width is estimated by the following equation:

$$\sigma_{v_i}^2 = \frac{\lambda^2}{4\hat{P}_i T_s^2} \sum_{k=-\frac{M}{2}}^{k_m + \frac{M}{2}} \hat{S}_i[\text{mod}_M(k)] \left(\frac{K}{M} + 2\hat{v}_D \frac{T_s}{\lambda} \right)^2 \quad (\text{II. 30})$$

K is the index of the strongest Fourier coefficient.

II.3.2 Polarimetric variables estimation:

As already mentioned, the signal power estimate is defined by:

$$\hat{S}_i = \hat{R}_i(0) - \hat{N}_i \quad (\text{II. 31})$$

II.3.2.1 Reflectivity factor:

It can be estimated by the following expression:

$$\hat{Z}_i(\text{dB}) = 10\log(\hat{S}_i) + 20\log(L) + 20\log(R) - 10\log(C) \quad (\text{II. 32})$$

Where:

L : One-way attenuation, R : range (m) and C : calibration constant ($\text{mm}^6 \text{m}^{-3}$), i is H or V channel.

II.3.2.2 Differential reflectivity:

Its estimation formula is:

$$\hat{Z}_{DR}(\text{dB}) = 10\log(\hat{S}_H) - 10\log(\hat{S}_V) \quad (\text{II. 33})$$

II.3.2.3 Correlation coefficient:

It is estimated by:

$$\hat{\rho}_{HV} = \frac{|\hat{R}_{HV}(0)|}{\sqrt{\hat{S}_H \hat{S}_V}} \quad (\text{II. 34})$$

II.3.2.4 Differential phase:

It can be estimated by:

$$\hat{\phi}_{DP} = \text{Arg}[\hat{R}_{HV}(0)] \quad (\text{II. 35})$$

II.4 Spectral polarimetric variables:

Spectral polarimetry is the combination of Doppler and polarimetric measurements so that the distribution of polarimetric variables be a function of radial velocity. They are defined from auto and cross spectra of signals from horizontal (H) and vertical (V) channels.

Known that:

$$S_i(f) = \int_{-\infty}^{\infty} R_i(l) e^{-i2\pi fl} dl \quad i = H, V \quad (\text{II. 36})$$

And the cross spectrum is defined by:

$$S_{HV}(f) = \int_{-\infty}^{\infty} R_{HV}(l) e^{-i2\pi fl} dl \quad (\text{II. 37})$$

Recall that $S_i(v)$ is related to $S_i(f)$:

The spectral differential reflectivity sZ_{DR} is defined as follows:

$$sZ_{DR}(v) = \frac{S_H(v)}{S_V(v)} \quad (\text{II. 38})$$

Z_{DR} is equivalent to the integration of spectral differential reflectivity $sZ_{DR}(v)$ weighted by normalized Doppler spectrum $S_{n,i}(v) = \frac{S_i(v)}{\int S_i(v)}$ [1][14] from V channel, the formula is given by:

$$Z_{DR}(v) = \int sZ_{DR}(v) S_{n,V}(v) dv \quad (\text{II. 39})$$

The spectral co-polar correlation coefficient and spectral differential phase are described in the following equations:

$$s\rho_{HV}(v) = \frac{|S_{HV}(v)|}{\sqrt{S_V(v)S_H(v)}} \quad (\text{II. 40})$$

$$s\varphi_{DP}(v) = \text{arg}[S_{HV}(v)] \quad (\text{II. 41})$$

ρ_{HV} is equivalent to the integration of $s\rho_{HV}(v)$ weighted by weighted by the square root of the product of normalized spectra from H and V channels, as shown in the following equation:

$$\rho_{HV} = \int s\rho_{HV}(v) \sqrt{S_{n,V}(v)S_{n,H}(v)} dv \quad (\text{II. 42})$$

II.5 Estimation of spectral polarimetric variables:

Using (II.17) the discrete Fourier transform (DFT) of M radar samples from H and V channels with hamming window $w(m)$ is writing as following [28]:

$$Z_i(f) = \sum_{m=0}^{M-1} w(m) V_i(m) e^{-j2\pi fm} \quad (\text{II. 43})$$

Where $f = kf_0$ ($k = 0, 1, \dots, M-1$), w is the weighting window (the window is used to reduce the side lobes of spectra).

The Doppler spectrum is estimated using the periodogram as shown in the following equation:

$$\hat{S}_i(f) = \frac{1}{M} |Z_i(f)|^2 = \frac{1}{M} \left| \sum_{m=0}^{M-1} w(m) V_i(m) e^{-j2\pi fm} \right|^2 \quad (\text{II. 44})$$

The cross spectrum is estimated by the following equation:

$$\hat{S}_{HV}(f) = \frac{\hat{S}_H(f)\hat{S}_V^*(f)}{M} \quad (\text{II. 45})$$

To reduce the variance in the spectrum estimator, the Doppler spectrum and cross-spectrum estimate are averaged over K sequences:

$$\bar{S}_i(f) = \frac{1}{K} \sum_{k=1}^K \hat{S}_i^k(f) \quad (\text{II. 46})$$

$$\bar{S}_{HV}(f) = \frac{1}{K} \sum_{k=1}^K \hat{S}_{HV}^k(f) \quad (\text{II. 47})$$

The spectra of polarimetric variables are represented as a function of radial velocity v ; by the relation between f and v ; the spectrum of the spectral differential reflectivity is estimated:

$$s\hat{Z}_{DR} = 10 \text{Log} \left(\frac{\bar{S}_H(v)}{\bar{S}_V(v)} \right) \quad (\text{II. 48})$$

Spectral co-polar correlation coefficient and spectral differential phase are estimated as following:

$$s\hat{\rho}_{HV}(v) = \frac{|\bar{S}_{HV}(v)|}{\sqrt{\bar{S}_V(v)\bar{S}_H(v)}} \quad (\text{II. 49})$$

$$s\hat{\varphi}_{DP}(v) = \text{arg}[\bar{S}_{HV}(v)] \quad (\text{II. 50})$$

Spectral polarimetry has been used to obtain microphysical information of precipitation as well as environmental parameters such as background wind and turbulence within the radar resolution volume.

II.6 Uncertainty of estimation:

It has been shown [2] [28] that the quality of the spectral polarimetric variables depends on many factors. In this work, the effects of some factors on the estimation of mean radial velocity, spectrum width, spectral differential reflectivity and spectral co-polar correlation coefficient have been verified by the following simulation.

The algorithm of this simulation is briefly summarized:

Step 1: generate K V-channel spectra randomly with a Gaussian shape and each spectrum has M samples. And for each sample over the K spectra, H-channel spectra is produced to meet the desired parameters $(\bar{v}_D, \sigma_v, sZ_{DR}, s\rho_{HV})$.

Step 2: apply IFFT for H and V-channel spectra to generate H and V time series of complex signal V_H, V_V for each K spectra.

Step 3: for more realistic signal, an independent noise is added for both H and V signal, based on desirable SNR.

Step 4: the spectral processing previously seen is applied on the noisy signal for the estimation [29].

The generated signal mimics the real radar signals as follows:

- wavelength $\lambda = 0.0938 \text{ m}$
- sampling period $T_s = 0.984 \text{ ms}$
- the non-ambiguous velocity $V_a = 23.831 \text{ m/s}$

II.6.1 Simulation of the first and second moment:

In this section, we analyze the perturbations of mean velocity and spectrum width estimations due to the SNR and the desired value of spectrum width for each method performed.

Using the auto-covariance processing:

We estimate the mean Doppler velocity and the spectrum width for $M = 64$ under these circumstances:

1. the desired spectrum width $\sigma_v = 2 \text{ m/s}$, the desired radial velocity $v_D = [-V_a \ V_a] \text{ m/s}$, and for different values of SNR: $SNR = -5 \text{ dB}$ in the left panel, $SNR = 5 \text{ dB}$ in the middle, $SNR = 20 \text{ dB}$ in the right panel, as shown in the figures:

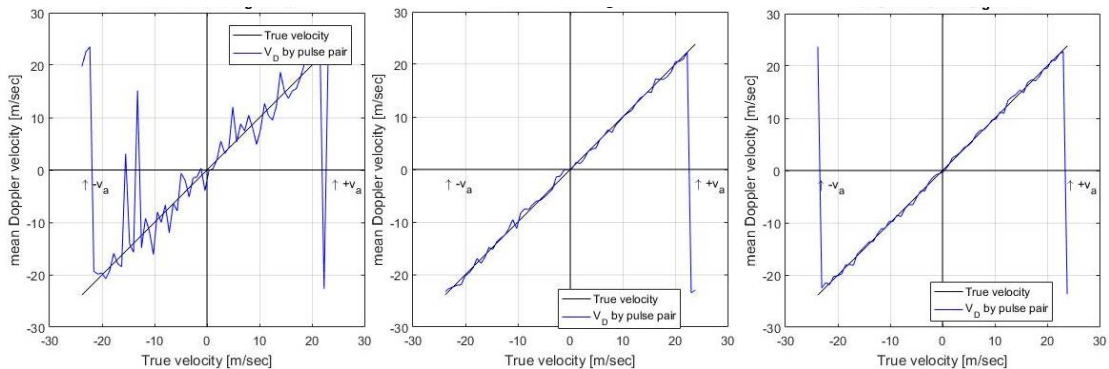


Figure II. 4: Mean Doppler velocity estimation, pulse pair method, for $SNR = -5 \text{ dB}$, $SNR = 5 \text{ dB}$, $SNR = 20 \text{ dB}$

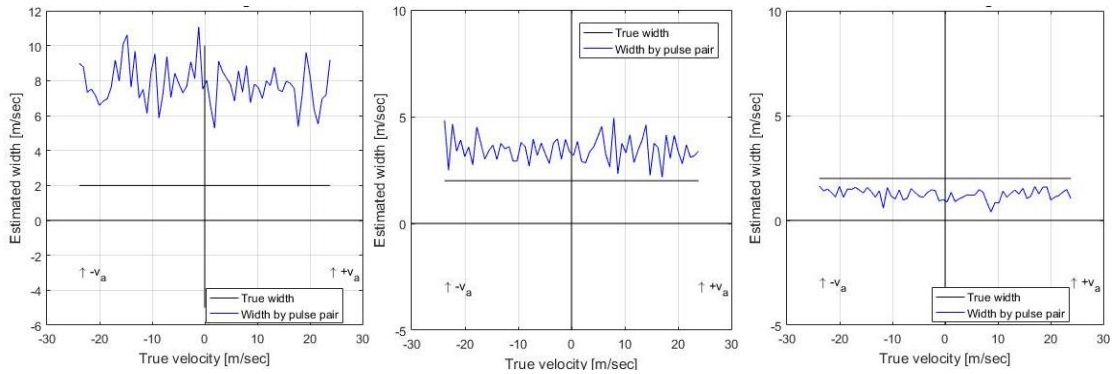


Figure II. 5 : Spectrum width estimation, pulse pair method, for $SNR = -5dB$, $SNR = 5dB$, $SNR = 20dB$

2. For different values of desired spectrum width: $\sigma_v = 0.2 m/s$ in the left panel, $\sigma_v = 2 m/s$ in the middle and $\sigma_v = 20 m/s$ in the right panel, the radial velocity $v_D = [-V_a \ V_a]m/s$, and $SNR = 20dB$, as shown in the figures:

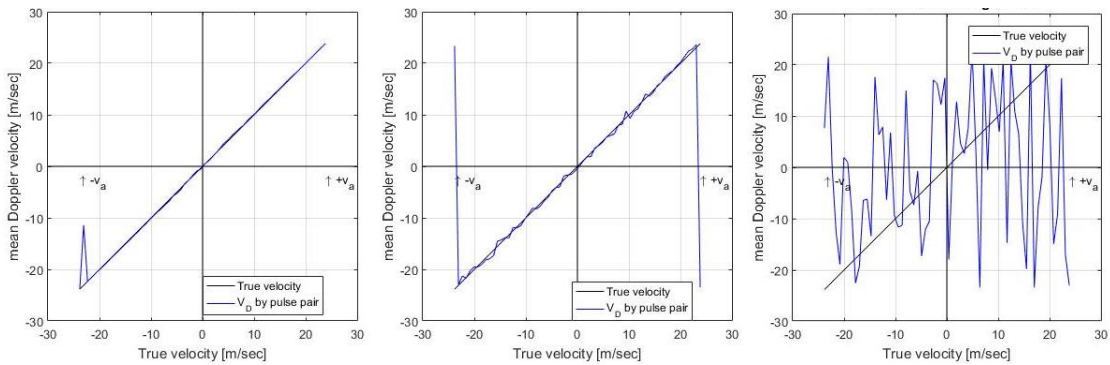


Figure II. 6: Mean Doppler velocity estimation, pulse pair method, for $\sigma_v = 0.2 m/s$, $\sigma_v = 2m/s$, $\sigma_v = 20 m/s$

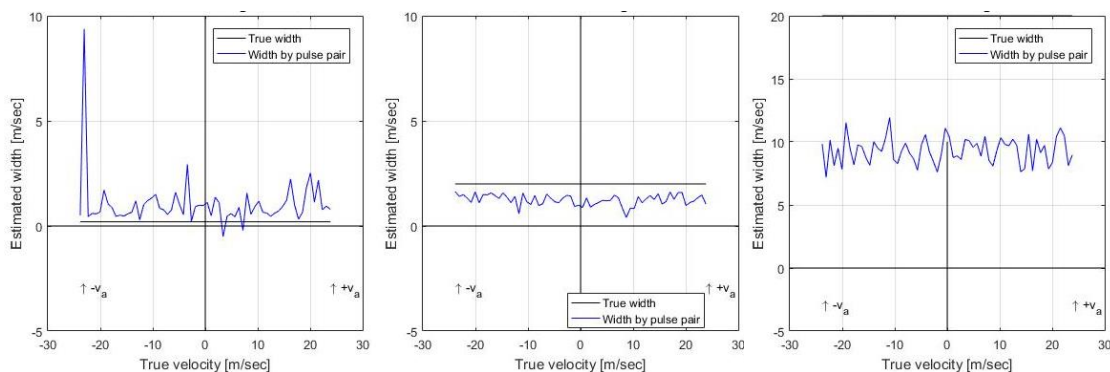


Figure II. 7 : Spectrum width estimation, pulse pair method, for $\sigma_v = 0.2 m/s$, $\sigma_v = 2m/s$, $\sigma_v = 20 m/s$

These figures indicate that the SNR and the spectrum width σ_v are the most important factors of errors. In other words, low SNR , narrow and very large spectrum width increase the uncertainty of spectrum width estimation, the estimation mean Doppler velocity is affected only by low SNR and very large spectrum width.

Using the spectral processing:

We estimate the mean radial velocity and spectrum width under the same circumstances in order to compare the two methods applied:

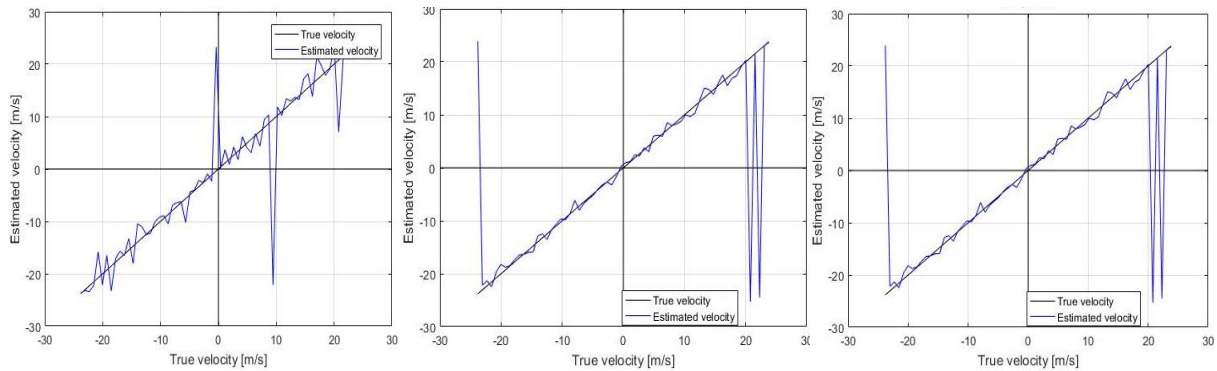


Figure II. 8 : Mean Doppler velocity estimation, spectral method, for $SNR = -5dB$ in the left $SNR = 5dB$ in the middle, $SNR = 20dB$ in the right

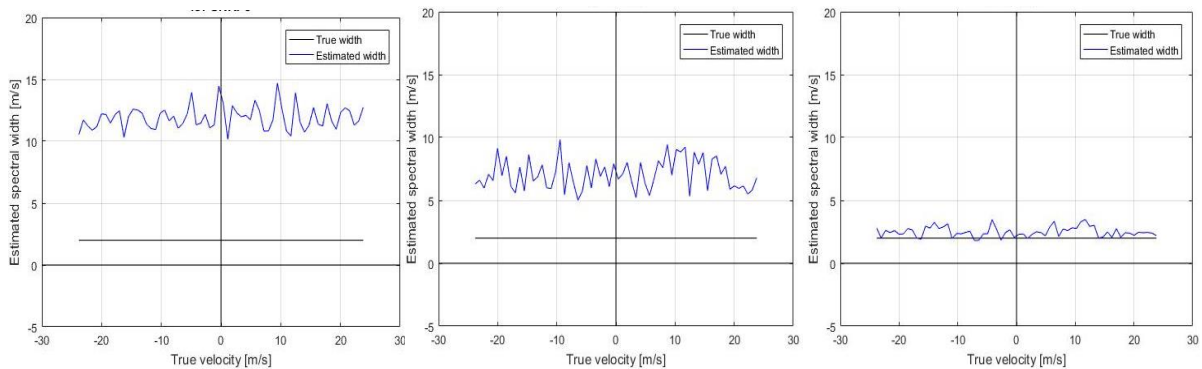


Figure II. 9: Spectrum width estimation, spectral method, for $SNR = -5dB$ in the left $SNR = 5dB$ in the middle, $SNR = 20dB$ in the right

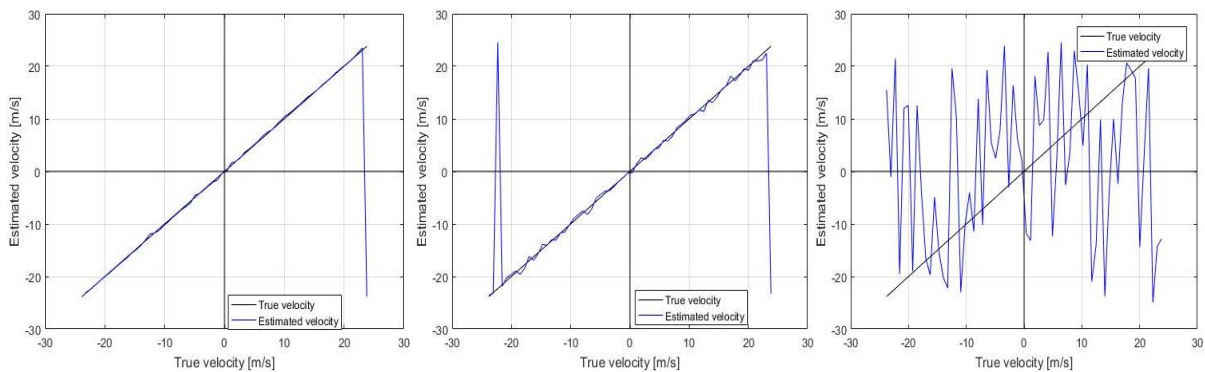


Figure II. 10: Mean Doppler velocity estimation, spectral method, for $\sigma_v = 0.2 \text{ m/s}$ in the left $\sigma_v = 2 \text{ m/s}$, in the middle $\sigma_v = 20 \text{ m/s}$, in the right

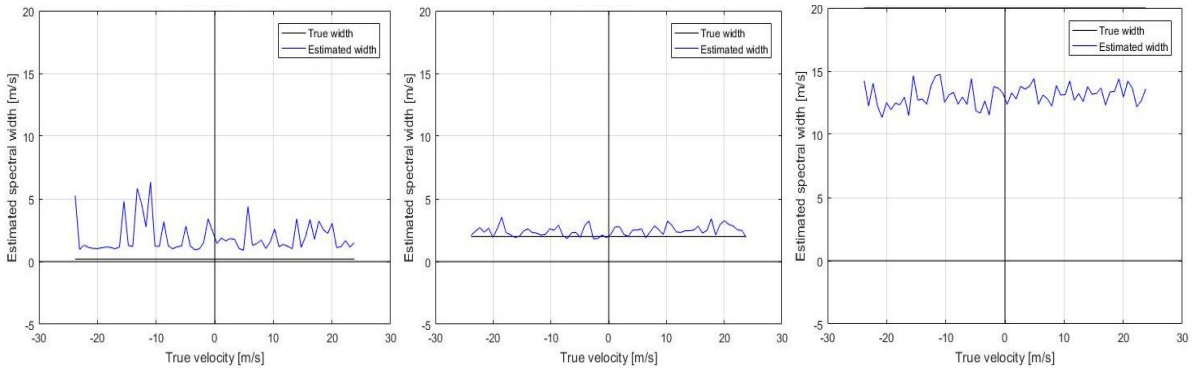


Figure II. 11: Spectrum width estimation, spectral method, for $\sigma_v = 0.2 \text{ m/s}$ in the left, $\sigma_v = 2 \text{ m/s}$, in the middle $\sigma_v = 20 \text{ m/s}$ in the right

We test the efficiency of this method by varying the number of samples, the results is shown in the figure bellow (for $M=64$ in the left panel, and $M=256$ in the right panel):

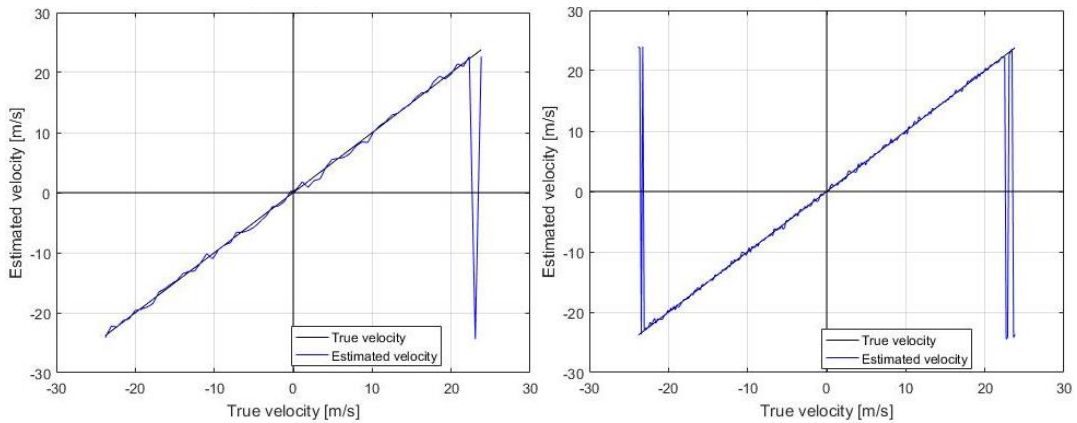


Figure II. 12: Mean Doppler velocity estimation, spectral method, for $M=64$ in the left, $M=256$ in the right

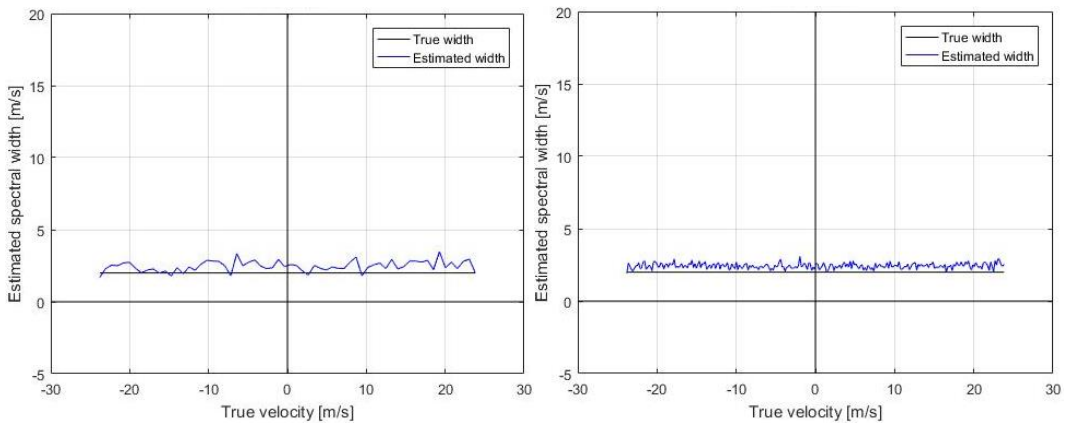


Figure II. 13: Spectrum width estimation, spectral method, for $M=64$ in the left, $M=256$ in the right

The factors already mentioned affect the estimation of spectral moments in the same way. The last figure shows that the number of samples must be large to provide the required accuracy.

II.6.2 Simulation of spectral of polarimetric variables:

This simulation verifies the effects of SNR, and the true ρ_{HV} on spectral differential reflectivity $s\hat{Z}_{DR}$ and the spectral co-polar correlation coefficient $s\hat{\rho}_{HV}$ estimation under these circumstances:

1. For $M = 64$, the desired $sZ_{DR} = 5dB$, the desired $\rho_{HV} = 0.99$, for various SNR: $SNR = -5dB$ in the left panel, $SNR = 5dB$ in the middle, $SNR = 20dB$ in the right panel, as shown in the figures:

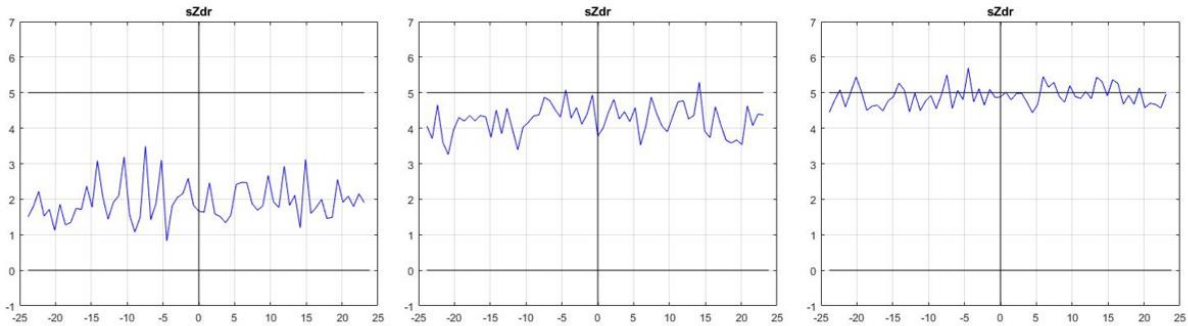


Figure II. 14: Spectral differential reflectivity estimates $s\hat{Z}_{DR}$ for $SNR = -5dB$, $SNR = 5dB$, $SNR = 20dB$

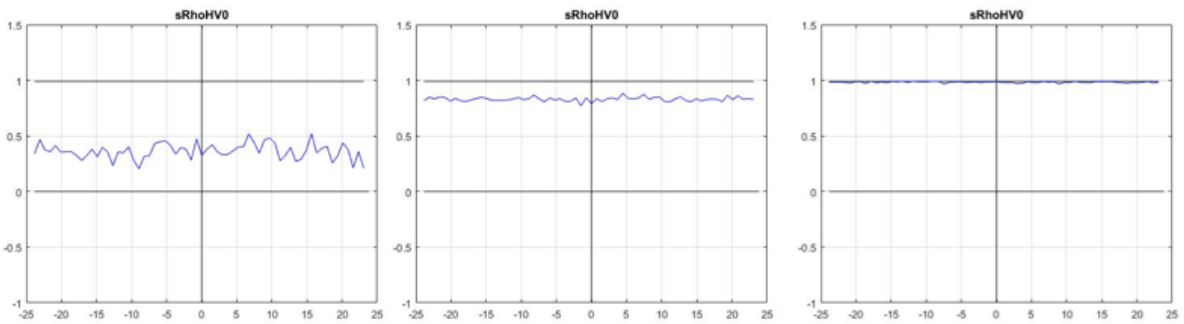


Figure II. 15: Spectral co-polar correlation coefficient $s\hat{\rho}_{HV}$ for $SNR = -5dB$, $SNR = 5dB$, $SNR = 20dB$

2. For $M = 64$, the desired $sZ_{DR} = 5dB$, for $SNR = 20dB$, for different values of desired: $\rho_{HV} = 0.8$ in the left panel, $\rho_{HV} = 0.9$ in the middle $\rho_{HV} = 0.95dB$ in the right panel, as shown in the figures:

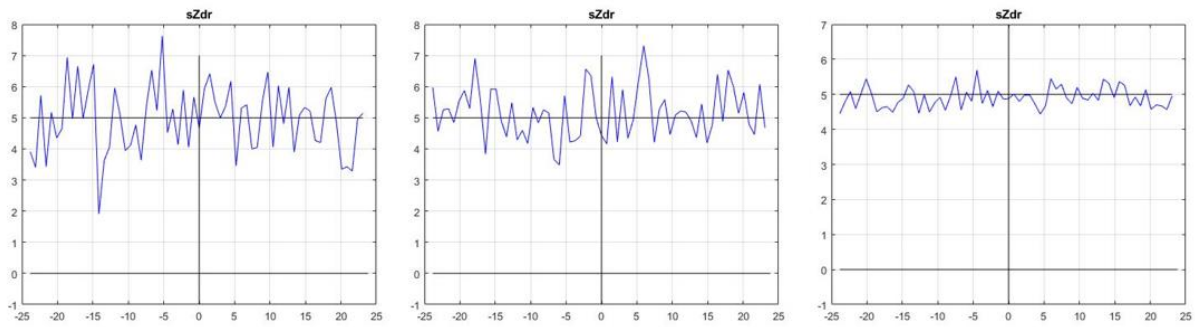


Figure II. 16: Spectral differential reflectivity estimates $s\hat{Z}_{DR}$ for $sp_{HV} = 0.8, sp_{HV} = 0.9, sp_{HV} = 0.99$

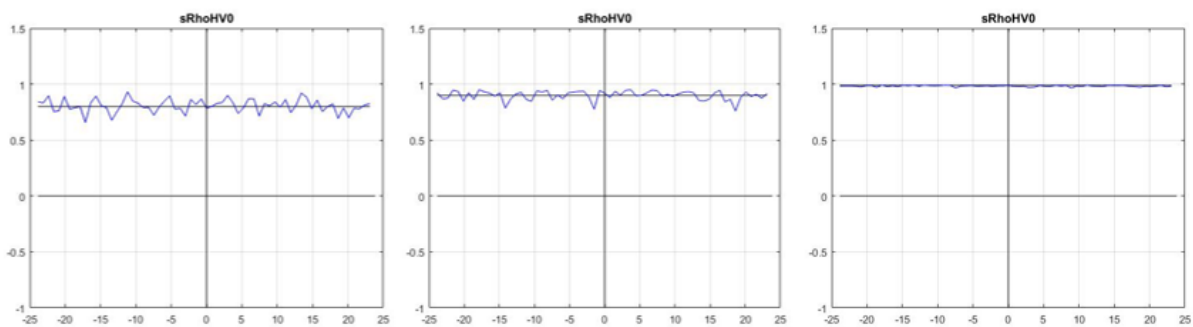


Figure II. 17: Spectral co-polar correlation coefficient estimates $s\hat{\rho}_{HV}$ for $sp_{HV} = 0.8, sp_{HV} = 0.9, sp_{HV} = 0.99$

The uncertainty of spectral differential reflectivity $s\hat{Z}_{DR}$ and the spectral co-polar correlation coefficient $s\hat{\rho}_{HV}$ estimation increase for: low SNR, large and low spectral correlation co-polar coefficient sp_{HV} . Yu and al (2012) [28] indicated that the accuracy of the estimate depends on the number of repetition, therefore to avoid this uncertainty it is necessary to increase this number.

Conclusion:

We have seen in this chapter, that polarimetric radars have many advantages they make possible to provide data of better quality than with conventional radars, the polarimetric data are also very interesting to characterize the microphysical properties of hydrometeors.

Chapter III: Shear induced size sorting and simulation

III.1 Introduction:

Polarimetric radars provide unique insight into microphysical processes in clouds and precipitation. Different microphysical processes (size sorting, evaporation, melting, freezing, etc.) are characterized by specific “polarimetric fingerprints” (e.g. Kumjian 2012) [30]. That can improve significantly the quality of radar estimates, which will be presented in this chapter.

III.2 Definition of size sorting:

The fall velocity of hydrometeors is dependent on their mass: larger, heavier particles tend to fall faster than smaller, lighter particles in quiescent conditions. This fall speed disparity leads to differential sedimentation of precipitating particles, resulting in transient size sorting. However, in nature, various types of atmospheric flows can maintain this otherwise transient size sorting, resulting in prolonged regions of ongoing particle sorting in precipitating storms. For example, consider the presence of a convective updraft or a vertical wind shear.

Trajectories for hydrometeors of different sizes are different depending on the microphysical and dynamical nature of a given precipitation system. Herein, we are concerned only by the size sorting that occurs in the presence of vertical shear of the horizontal wind.

Precipitation particles which fall aloft through a wind shear are sorted as to size, the largest particles reaching the ground, the smaller particles further from it. If precipitation is assumed to form continuously in cloud, with a fixed size distribution, this sorting affects significantly the size distributions (DSD) [31].

III.3 Equation of movement under shear:

The motion equation of hydrometeor in presence of shear is related to air flow. It was derived in many previous studies, such as Brussaard (1974, 1976), Bohne (1982), and Beard and Jameson (1983). [17] [32] [33]

We Consider gravity and drag as the principal forces. In the horizontal direction \vec{a}_h , and the vertical direction \vec{a}_z ; \vec{a}_z is upward; the velocity of hydrometeor of size D is: $U(t) = V_h \vec{a}_h + V_z \vec{a}_z$.

At height H where the hydrometeor is located, its velocity is equal to wind velocity $\vec{U}(t) = \vec{a}_h U_h$.

According to the Newton's second law, the net force is given by:

$$\vec{F}_n = \vec{F}_g + \vec{F}_d \quad (\text{III. 1})$$

With:

$F_g = mg$: is the gravity force, m is the mass and $\vec{g} = \vec{a}_h \cdot 0 + \vec{a}_z(-g)$, g is the gravity, we obtain $\vec{F}_g = -g\vec{a}_z$.

And \vec{F}_d is the drag force (air resistance) derived by Bohne, 1982 by this equation:

$$\vec{F}_d = -m \frac{\vec{v} - \vec{U}}{\tau} \quad (\text{III. 2})$$

Where: $\tau = \frac{V_t(D)}{g}$ is the time constant, reminder $V_t(D)$ is the terminal velocity.

Thus the equation (III.1) becomes:

$$\begin{aligned} \frac{d\vec{V}}{dt} &= \vec{g} - \frac{\vec{V}(t) - \vec{U}(t)}{\tau} \\ \frac{d\vec{V}}{dt} + \frac{\vec{V}(t)}{\tau} &= \vec{g} + \frac{\vec{U}(t)}{\tau} \end{aligned} \quad (\text{III. 3})$$

To solve this first order differential equation, we multiply both sides of (III.3) by $e^{t/\tau}$:

$$\frac{d\vec{V}}{dt} e^{t/\tau} + \frac{\vec{V}(t)}{\tau} e^{t/\tau} = \vec{g} e^{t/\tau} + \frac{\vec{U}(t)}{\tau} e^{t/\tau} \quad (\text{III. 4})$$

Integrating (III.4) with respect to t' from 0 to t :

$$\begin{aligned} \int_0^t \frac{d}{dt'} (\vec{V}(t') e^{t'/\tau}) dt' &= \int_0^t \vec{g} e^{t'/\tau} dt' + \int_0^t \frac{\vec{U}(t')}{\tau} e^{t'/\tau} dt' \\ \vec{V}(t) e^{t/\tau} - \vec{V}(0) &= \vec{g} \tau (e^{t/\tau} - 1) + \int_0^t \frac{1}{\tau} \vec{U}(t') e^{t'/\tau} dt' \\ \vec{V}(t) &= \vec{V}(0) e^{-t/\tau} + \vec{g} \tau (1 - e^{-t/\tau}) + e^{-t/\tau} \int_0^t \frac{1}{\tau} \vec{U}(t') e^{t'/\tau} dt' \end{aligned} \quad (\text{III. 5})$$

To solve $\int_0^t \frac{U(t')}{\tau} e^{t'/\tau} dt'$, we need the derivation of $U(t')$ for that. Note that vertical shear constant $s = \frac{dU_h}{dz}$, and the variation of height with time is the terminal velocity then:

$$\frac{d\vec{U}(t)}{dt} = \frac{d\vec{U}(t)}{dh} \frac{dh}{dt} = s V_t(D) \vec{a}_h \quad (\text{III. 6})$$

Integrating the equation (III.6) in the aim to obtain $U(t)$:

$$\int_0^t \frac{d\vec{U}(t')}{dt'} dt' = \int_0^t sV_t(D)\vec{a}_h dt'$$

$$\vec{U}(t) = (\vec{U}(0) + sV_t(D)t)\vec{a}_h \quad (\text{III. 7})$$

The integral $\int_0^t \frac{U(t')}{\tau} e^{t'/\tau} dt'$ can turn into:

$$\frac{e^{-t/\tau}}{\tau} \int_0^t \vec{U}(t') dt' = \frac{e^{-t/\tau}}{\tau} \int_0^t (\vec{U}(0) + \vec{a}_h sV_t(D)t) e^{t'/\tau} dt'$$

$$\frac{e^{-t/\tau}}{\tau} \int_0^t \vec{U}(t') dt' = \vec{U}(0) (1 - e^{-t/\tau}) + \vec{a}_h sV_t(D) (t - \tau + \tau e^{-t/\tau}) \quad (\text{III. 8})$$

This result (III.8) is substituted in the equation (III.5):

$$\vec{V}(t) = \vec{V}(0)e^{-t/\tau} + \vec{g}\tau (1 - e^{-t/\tau}) + \vec{U}(0) (1 - e^{-t/\tau}) + \vec{a}_h sV_t(D) (t - \tau + \tau e^{-t/\tau})$$

According to Bohne, 1982, typically τ is relatively very small, (i.e. $\tau \ll t$; $e^{-t/\tau} \approx 0$), although:

$$\vec{V}(t) = \vec{g}\tau + \vec{U}(0) + sV_t(D)(t - \tau)\vec{a}_h \quad (\text{III. 9})$$

Replacing $\vec{U}(0)$ from (III.7) in (III.9) we obtain:

$$\vec{V}(t) = \vec{U}(t) - (sV_t(D)\tau)\vec{a}_h + \tau\vec{g} \quad (\text{III. 10})$$

Therefore, the hydrometeor's horizontal and vertical velocity components can be derived as (recall that $\tau = \frac{V_t(D)}{g}$):

$$\vec{V}_h(t) = (U_h(t) - \frac{sV_t^2(D)}{g})\vec{a}_h \quad (\text{III. 11})$$

$$\vec{V}_z(t) = -V_t(D)\vec{a}_z \quad (\text{III. 12})$$

The initial horizontal velocity of a single falling hydrometeor is assumed to be the same as horizontal wind speed \vec{U} . The initial vertical velocity of the drop is assumed to be zero.

III.4 Canting angle under shear:

The canting angle previously seen in equation (I. 38) is described by:

$$\tan\gamma = -\frac{1}{g} \frac{dV_h}{dt}$$

A new formula of γ can be derived from (III.11) and (III.6), it is given by:

$$\tan\gamma = -\frac{1}{g} sV_t(D) \quad (\text{III. 13})$$

As the following figure shows, the different cases of wind shear can change the orientation drops:

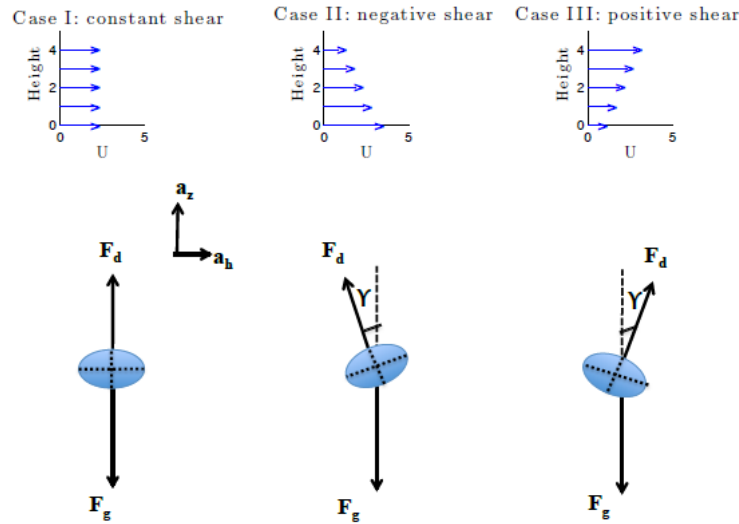


Figure III. 1: canting angle under shear

If no shear is present, the constant wind can only change the trajectory of the hydrometeor, but will not change its orientation (i.e. canting angle is zero). On the other hand, if shear is present, not only the hydrometeor's trajectory will change, but also the orientation of the hydrometeor will change to balance with the surrounding air flow. Beard and Jameson, 1983 studied the impact of canting angle on Z_{DR} , they demonstrated that the change of orientation of a canted drop can affect the returned signal. [34]

Although undetectable to single-polarization radars, size sorting can have an impact on dual-polarization radar observations, producing signatures on reflectivity and differential reflectivity spectrum that can be broadened by turbulence.

III.5 Doppler spectrum in turbulence environment:

The Doppler spectrum for n types of hydrometeors broadened by turbulence is derived by Yanovsky, 2011 as follows: [35]

$$S_i(v) = S'_i(v) * S_b(v) \quad (\text{III. 14})$$

Where:

$S_b(v)$: The Kernel turbulence broadening which is modeled by a Gaussian

function:
$$S_b(v) = \frac{1}{\sqrt{2\pi}\sigma_v} e^{-\frac{v^2}{2\sigma_v^2}},$$

(*): is the convolution operator,

$S'_i(v)$: is the Doppler spectrum for n types of hydrometeors for H and V channel, derived as follows [36] [37]:

$$S'_i(v) = \sum_{j=1}^n N_j [D_j(v)] \sigma_{i,j} [D_j(v)] \left| \frac{dD_j}{dv} \right| \quad (\text{III. 15})$$

$\left| \frac{dD_j}{dv} \right|$ is the Jacobian of diameter to velocity, $N_j [D_j(v)]$ is the DSD of each type, $\sigma_{i,j} [D_j(v)]$ is backscattering cross section.

III.6 Backscattering cross section:

The matrix of backscattering cross section obtained from the scattered signal is:

$$\sigma = \begin{vmatrix} \sigma_{HH} & \sigma_{HV} \\ \sigma_{VH} & \sigma_{VV} \end{vmatrix} \quad (\text{III. 16})$$

The radar cross section is defined as 4π times the scattering amplitude of the horizontal and vertical polarization $\langle |F_H|^2 \rangle$ and $\langle |F_V|^2 \rangle$ respectively (in mm^2m^{-3})

$$\sigma_{ii} = 4\pi \langle |F_i|^2 \rangle \quad i = H \text{ or } V \quad (\text{III. 17})$$

Where:

$$\begin{aligned} \langle |F_H|^2 \rangle &= \langle (Af_a + Bf_b)(Af_a + Bf_b)^* \rangle \\ &= \bar{A}^2 \langle |f_a|^2 \rangle + \bar{B}^2 \langle |f_b|^2 \rangle + 2\bar{A}\bar{B} \langle f_a f_b^* \rangle \end{aligned} \quad (\text{III. 18})$$

$$\begin{aligned} \langle |F_V|^2 \rangle &= \langle (Cf_a + Df_b)(Cf_a + Df_b)^* \rangle \\ &= \bar{C}^2 \langle |f_a|^2 \rangle + \bar{D}^2 \langle |f_b|^2 \rangle + 2\bar{C}\bar{D} \langle f_a f_b^* \rangle \end{aligned} \quad (\text{III. 19})$$

The values of \bar{A}^2 , \bar{B}^2 , \bar{C}^2 and \bar{D}^2 are functions of the elevation angle θ and properties of canting angle γ , given by the following equations:

$$\bar{A}^2 = A_0 + \sin^4 \gamma B_0 + 2\sin^2 \gamma C_0 \quad (\text{III. 20})$$

$$\bar{B}^2 = \cos^4 \gamma B_0 \quad (\text{III. 21})$$

$$\bar{C}^2 = \cos^4 \gamma A_0 \quad (\text{III. 22})$$

$$\bar{D}^2 = B_0 + \sin^4 \gamma A_0 + 2\sin^2 \gamma C_0 \quad (\text{III. 23})$$

And:

$$A_0 = \frac{1}{8} (3 + 4\cos 2\bar{\gamma} e^{-2\sigma^2} + \cos 4\bar{\gamma} e^{-8\sigma^2}) \quad (\text{III. 24})$$

$$B_0 = \frac{1}{8} (3 - 4\cos 2\bar{\gamma} e^{-2\sigma^2} + \cos 4\bar{\gamma} e^{-8\sigma^2}) \quad (\text{III. 25})$$

$$C_0 = \frac{1}{8} (1 - \cos 4\bar{\gamma} e^{-8\sigma^2}) \quad (\text{III. 26})$$

Where: $\bar{\gamma}$ and σ are the mean and SD of canting angle.

A numerical method; (T matrix method) allows us to calculate the amplitudes of scattering f_a and f_b for rain and hail drops (Zhang et al. 2001) [38]. Due to its complexity a simpler analytic method is used in this work: [3] [4]

As hydrometeor size is smaller compared to wavelength λ , that allows us to use Rayleigh approximation, so scattering amplitudes f_a, f_b are given by:

$$f_{a,b} = \frac{\pi^2 D^3}{6\lambda^2} \frac{1}{L_{a,b} + \frac{1}{\varepsilon - 1}} \quad (\text{III. 27})$$

Where ε is dielectric constant ($\varepsilon_w = 70.9 - 29.4j$ for rain at 10°C, $\varepsilon_H = 22.6 - 11.41j$ for hail for melting ratio $f_w = 0.4$) and D is equivolume diameter, L_a, L_b are the shape parameters defined as:

$$L_a = \frac{1+f^2}{f^2} \left(1 - \frac{atanf}{f}\right), f = \sqrt{\beta^2 - 1}, L_b = \frac{1-L_a}{2} \quad (\text{III. 28})$$

With β is the axis ratio defined in the chapter 1.

III.7 Simulation:

Past studies using spectral polarimetry mainly relied on size sorting originating from hydrometeors different terminal velocities has focused at high elevation angle for example Spek et al. (2008) which applied spectral polarimetry to S-band data collected at 45° elevation angle, and Moisseev et al. (2006) applied spectral polarimetry to estimate the shape parameter of raindrops using data from the S-band CSU-CHILL at elevation of 30° and the S-band Transportable Atmospheric Radar (TARA) at 45°. [39]

In this work, numerical simulation considers the shear-induced size sorting mechanism is developed for a mixture of hydrometeor's types (rain and hail), in turbulence at C-band at 0° elevation angle, based on the work developed in Wang (2010).

The inputs of simulation are shear (s), elevation angle θ , turbulence broadening σ_b , melting ratio f_w , the parameters of DSD for both rain and hail, and SNR . The main idea is to generate Doppler spectrum from both H and V channels for individual hydrometeor type separately from shear-induced size sorting, then the procedure is repeated to the next type of hydrometeors, and resulting Doppler spectra for H and V channels are the summations of individual spectra from each hydrometeor type and broadened by turbulence, the output of simulation is reflectivity, differential reflectivity spectra for all types for hydrometeors with the same polarization.

The steps of simulation:

1. Calculate DSD using the equations (I.37) for rain and (I.46) for hail, after providing range of sizes D_w, D_H .
2. Calculate the radial velocity from shear-induced size sorting:
 - a. Calculate the terminal velocity over the range of size sorting using (I.35) for rain, (I.45) for hail.
 - b. Deduce the horizontal and vertical velocities with the given equations (III.11), (III.12) and the shear is obtained from the inputs.
 - c. Project the velocities to obtain the radial velocity to the beam direction given the elevation angle $v = V_h \cos \theta + V_z \sin \theta$.
3. Calculate the backscattering cross section:
 - a. Obtain f_a and f_b from (III.27)
 - b. Obtain the mean and standard deviation of canting angle, 0° for rain and $5^\circ(1 - 0.8f_w)$ for hail (for given melting ratio f_w).
 - c. Calculate the scattering amplitude of horizontal and vertical polarization using (III.17).
4. Calculate the Doppler spectrum for both horizontal and vertical channel, equation (III.15).
5. Resample the spectra to uniform range of radial velocities.
6. Add the turbulence broadening using (III.14).
7. Repeat Step 1 - 7 for the next types of hydrometeor.
8. Input SNR to calculate the noise power with the given equation:

$$sSNR_i(v) = \frac{s\bar{S}_i(v)}{N_i(v)}$$

Then add it to the spectra for both H and V channels

9. Calculate differential reflectivity spectrum using (II.38).

By changing inputs values one by one, while keeping the others constant, a good insight is obtained on the dependence of the spectral reflectivity and differential reflectivity on the parameters of DSD and dynamic environment proprieties (shear, turbulence broadening and wind velocity). Here we only present the cases where a significant change is observed.

Before starting analysis, it must be noted that: the size of hydrometeors increases as for left to right in plots, in other word the smallest raindrops produces the lowest velocity values (approximately -15 m s^{-1}) and the largest hails produce radial velocity of approximately zero, that is due to the combination of negative shear and negative horizontal wind [6].

The initial inputs are:

- Hail DSD: $D_H = [5.2 - 25 \text{ mm}]$, $\Lambda = 0.4$, $N_0^h = 100$, $f_w = 0.4$
- Rain DSD: $D_R = [0.08 - 8 \text{ mm}]$, $D_0^R = 3.8$, $\mu = 3$, $N_0^R = 3000$
- Dynamic environment's properties: $U = -10 \text{ m} \cdot \text{s}^{-1}$, $s = -0.025 \text{ s}^{-1}$, $\sigma_b = 1$

The plots are shown in the following figures ($\hat{S}_H(v)$ in the left panel $s\hat{Z}_{DR}(v)$ in the right panel):

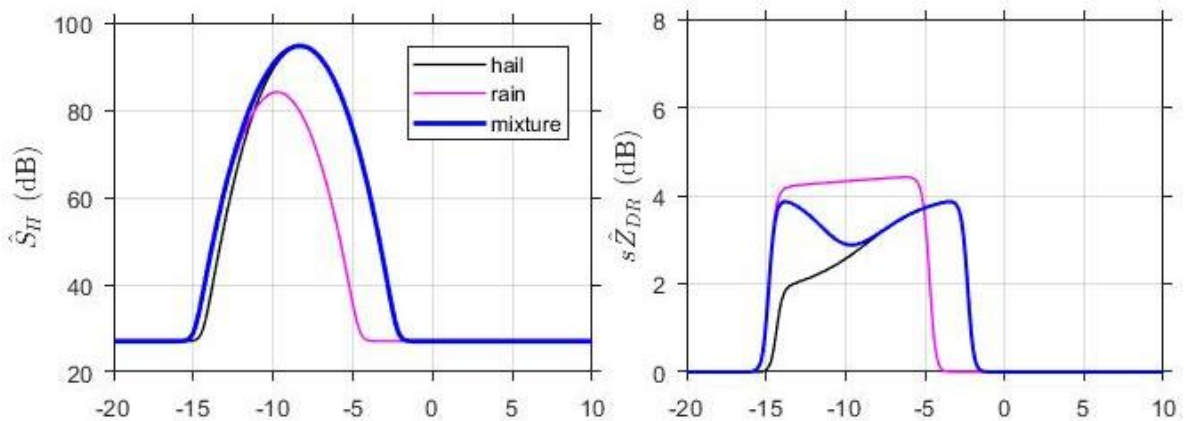


Figure III. 2 : The reference plots

As shown in figure, the resulted Doppler spectra have a range from approximately -15 to 0 m s^{-1} . Spectral reflectivity of all types has value of 80 dB and melting hail $s\hat{Z}_{DR}$ has value between $2 - 4 \text{ dB}$ with a positive slope. On the other hand, $s\hat{Z}_{DR}$ slope from raindrop is almost flat with a value of approximately 4.5 dB .

The $s\hat{Z}_{DR}$ from the mixture has a curve shape with value between 3 – 4dB. The spectra are centered on the radial component of background wind $U = -10m.s^{-1}$, at $v = -15m/s$, $s\hat{Z}_{DR}$ spectrum is dominant by raindrop, at $v = -5 \sim 0m/s$ it is dominant by hail, so it's consistent with what was mentioned before.

For different environment's properties (assuming a very small values of s , σ_b): $U = -10m.s^{-1}$, $s = -0.0015$, $\sigma_b = 0.5$ in the top panels, and $U = -10m.s^{-1}$, $s = -0.025s^{-1}$, $\sigma_b = 0.5$ in the bottom:

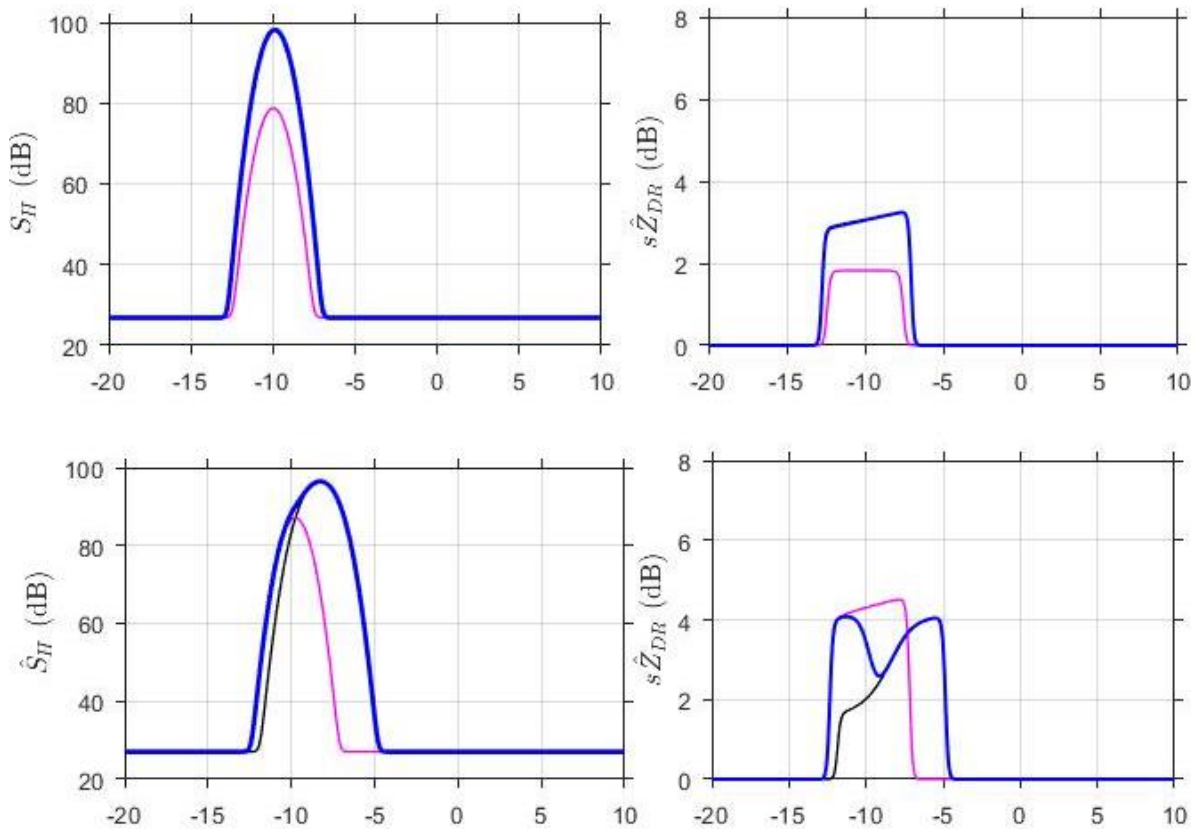


Figure III. 3 : Plots for different environment's properties

Assuming very small s , σ_b means no shear and nonturbulence environment: a flat and narrow $s\hat{Z}_{DR}$ and narrow \hat{S}_H spectra are obtained, and $s\hat{Z}_{DR}$ values are very small, comparing to the reference plot. For this case, spectral polarimetry does not provide additional information than the convectional polarimetric variables.

If only turbulence broadening is weaker, narrow spectra are shown; $s\hat{Z}_{DR}$ slope becomes steeper; which is consistent with (Yanovsky, 2011) study.

After a series of attempts with different values of DSD parameters, three cases where a slope change is observed are chosen to deduce the signatures of rain and hail size distribution on spectral reflectivity and differential reflectivity:

Case 1: considering mixture of large raindrops ($D_w = [5.2 - 8mm]$), and fewer large melting hails ($\Lambda = 0.7$) and keeping other parameters with the initial values.

Case 2: considering the mixture of dominating rain and a fewer large melting hail (by decreasing N_0^h from 100 to 10, $\Lambda = 0.7$ and increasing N_0^R from 3000 to 5000 while keeping other parameters with the initial values.

Case 3: considering mixture of more number of large hail ($\Lambda = 0.4$), and less raindrop concentration (by reducing N_0^R to 1000).

The results are presented in the following plots:

Case 1:

- Hail DSD: $D_H = [5.6 - 25mm]$, $\Lambda = 0.7$, $N_0^h = 100$, $f_w = 0.4$
- Rain DSD: $D_R = [5.2 - 8mm]$, $D_0^R = 3.8$, $\mu = 3$, $N_0^R = 3000$
- Dynamic environment properties: $U = -10m.s^{-1}$, $s = -0.025s^{-1}$, $\sigma_b = 1.5$

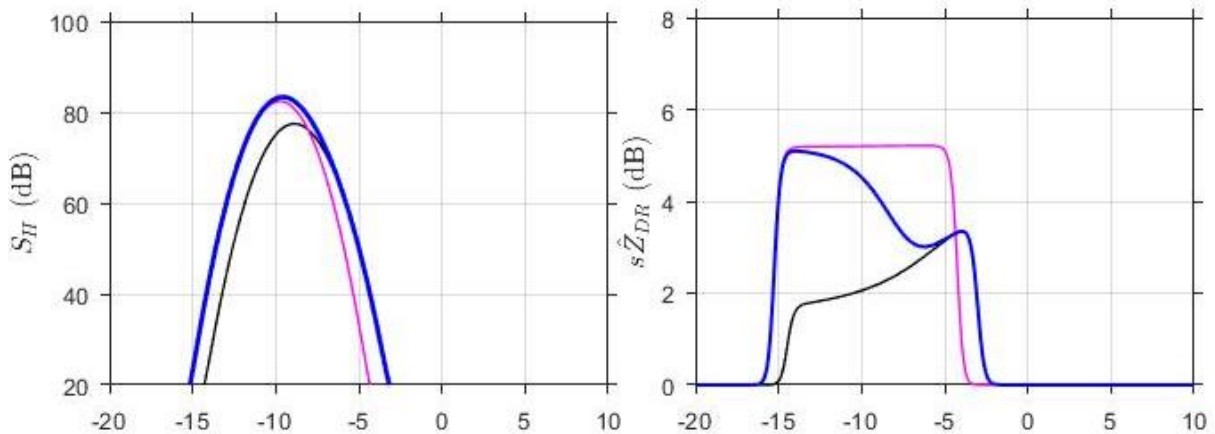


Figure III. 4 : Plots under the first case

Case 2:

- Hail DSD: $D_H = [5.6 - 25mm]$, $\Lambda = 0.7$, $N_0^h = 10$, $f_w = 0.4$
- Rain DSD: $D_R = [5.2 - 8mm]$, $D_0^R = 3.8$, $\mu = 3$, $N_0^R = 5000$
- Dynamic environment properties: $U = -10m.s^{-1}$, $s = -0.025s^{-1}$, $\sigma_b = 1.5$

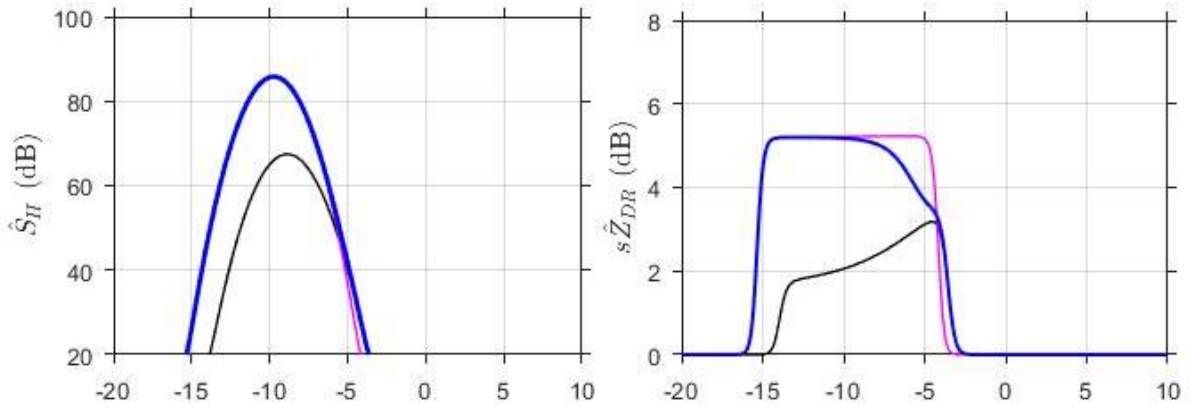


Figure III. 5 : Plots under the second case

Case 3:

- Hail DSD: $D_H = [5.6 - 25mm]$, $\Lambda = 0.7$, $N_0^h = 100$, $f_w = 0.4$
- Rain DSD: $D_w = [0.08 - 8mm]$, $D_0^R = 3.7$, $\mu = 3$, $N_0^R = 1000$
- Dynamic environment properties: $U = -10m.s^{-1}$, $s = -0.025s^{-1}$,

$$\sigma_b = 1.5$$

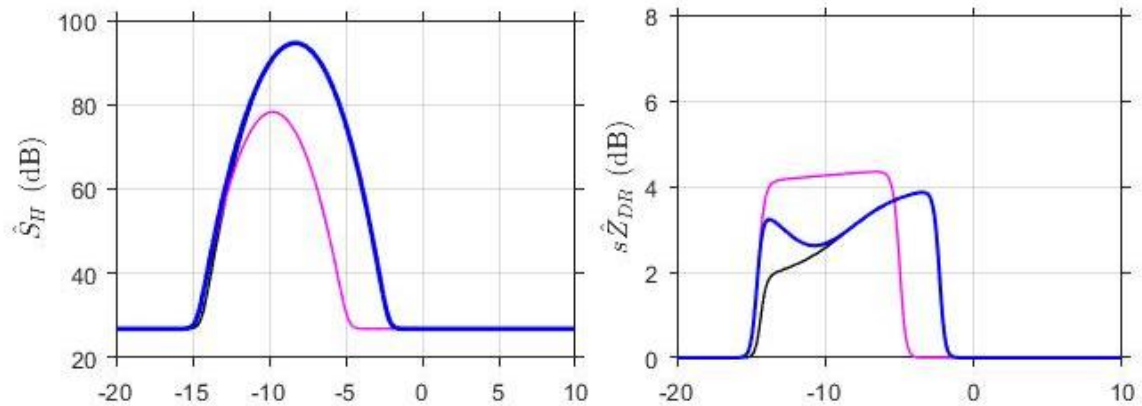


Figure III. 6 : Plots under the third case

Herein, we are interested only by slope of spectral differential reflectivity from mixture because it shows significantly different values. In the first case, negative slope of $s\hat{Z}_{DR}$ for mixture is resulted because of highest value at $-15 m s^{-1}$ contributed from large raindrops, and lowest value at $-2 m s^{-1}$ from large melting hail.

In the second one, large value of $s\hat{Z}_{DR}$ with zero slope is resulted because, melting hail which is less concentrated are well mixed with dominating rain in strong turbulent condition.

In the last circumstance, positive slope is mainly contributed from large melting hail, and smaller amount of raindrops which produce low $s\hat{Z}_{DR}$ on the left side at -15 m s^{-1} .

Conclusion:

The goal of this simulation is to explain how to deduce the types of hydrometeors, their concentrations and the dynamic environmental conditions in the resolution volumes using spectral differential reflectivity.

Finally, we got a polarimetric spectrum model to investigate hail signature in a hailstorm appeared at the low elevation angle.

Chapter IV: Application of the results on a hailstorm

IV.1 Introduction:

From previous chapters, polarimetric variables such as differential reflectivity, correlation coefficient, and differential phase can provide information about hydrometeor's size, shape, concentration, orientation, and type. In addition, the kinematic information such as storm intensity, motion, and turbulence can also be derived from Doppler measurements of mean radial velocity and spectrum width. Spectral polarimetry on the other hand, can unveil the polarimetric variables directly as a function of radial velocities within one resolution volume and this provides a unique opportunity to relate storm microphysical properties to kinematics, and dynamics.

The purpose of this chapter is to examine C-band polarimetric data from a unique hailstorm using abundant ground truth for this event. Then spectral polarimetry is applied to observation of hailstorm core at the low elevation angle in order to better understand and to gain more information about hailstorm properties.

IV.2 C-band radar observations and Application of spectral polarimetry on the 24 April 2011 Oklahoma City Extreme Hailstorm:

IV.2.1 Event description:

April 2011 was one of the most active, destructive, and deadly tornado months on record for the United States. From NOAA, 40 hailstorm events were reported over Oklahoma starting at 6:04 UTC in Jefferson, on 24 April 2011 and ending at 4:09 UTC in Tulsa on 25 April 2011. A total of 19 counties were affected by hails with size ranging from 1.9 to 7.0 cm. The cold front along the high way I-44 one day before, (i.e., on 23 April 2011), moved slowly toward southwest through central Oklahoma. A combination of surface heating, and lifting associated with the front helped the development of severe thunderstorms in early evening over southeast Oklahoma on the 24 April. Thunderstorms moved from southwest into central Oklahoma. At 18:50 UTC 24 April 2011, a hailstorm was crossing through Rush Spring and ACME. In both these areas, hails were reported with size of 1.9 cm. Only these two locations are located close to the azimuth angle of OU-PRIME RHI scan.

IV.2.2 DATA collection:

Information on wind surface condition and temperature from Norman sounding data at 19:00 UTC is presented in the figure (IV.1):

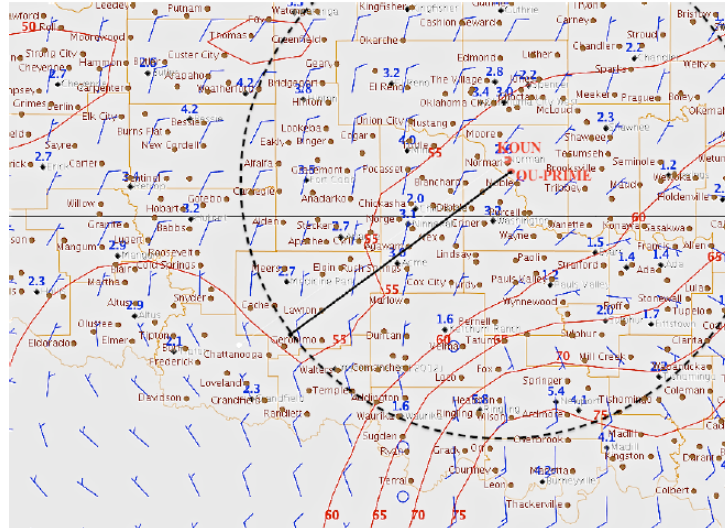


Figure IV 1: Surface conditions from Mesonet measurements at 19:00 UTC 24 April 2011 over central Oklahoma.

- The black dashed line: indicates the maximum range of 127 km for OU-PRIME observation.
- The black solid line: represents the beam direction at azimuth angle of 233.3° (where the hail was reported).
- The blue bars: represents the interpolated wind data at the height of 2 m, and the wind speed at 2-m height at these stations are also displayed.
- The red contours: represents interpolated air temperature (red contours) at the height 1.5 m, along of this OU-PRIME radial, a change of temperature can be observed around Rush Spring, where hail was reported at 18:50 UTC.

The wind velocity at 19:00 UTC is interpolated to the OU-PRIME radial of 233.3° and the results of maximum wind speed, wind direction and the horizontal shear are presented in the figure below:

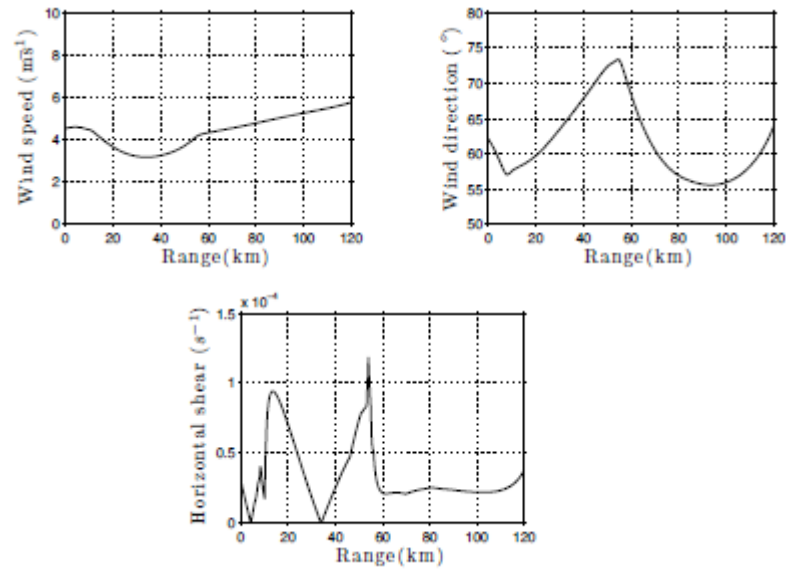


Figure IV 2: maximum wind speed, wind direction and the horizontal shear (from interpolated Mesonet wind data at 19:00 UTC.)

It can be observed that a variation of both wind speed and direction along the radial is relatively small. The wind and temperature profiles from radiosonde at 19:00 UTC from the Norman site are shown:

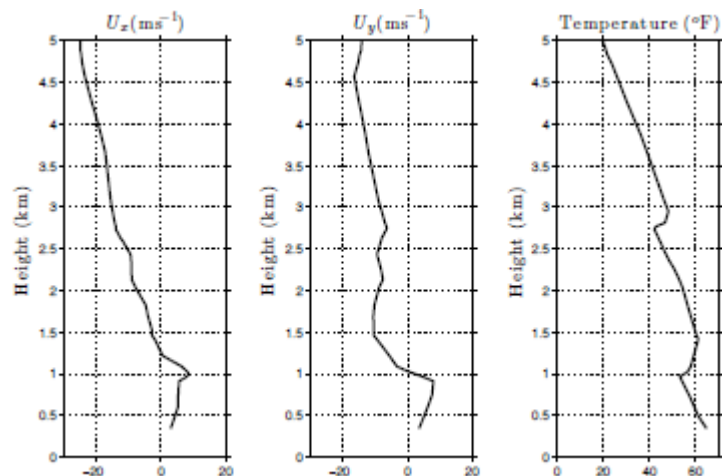


Figure IV 3 : Norman sounding data with zonal wind U_x , meridional wind U_y and air temperature at 00 UTC on 24 April 2011. (from Mesonet station)

An indication of vertical shear can be observed at lower altitude, which is favorable for the development of thunderstorm (lower than 1 km).

IV.3 Radar observations of hailstorm:

IV.3.1 Radar specification:

Data were collected by a Polarimetric radar OU-PRIME in Oklahoma, on 24 April 2011 between 17:00:13 UTC and 19:59:49 UTC.

The C-band research radar OU-PRIME, is operated by the Atmospheric Radar Research Center at the University of Oklahoma. It uses the “SHV” operation mode, in which the horizontally and vertically polarized waves are transmitted and received simultaneously. OU-PRIME data were collected using a sector scanning strategy within a 938 azimuthal interval with 8 elevation angles, allowing for more rapid updates.

RADAR	OU-PRIME
Wavelength (cm)	5.44
Antenna beamwidth (°)	0.45
Peak transmitter (MW)	1
Radial resolution (m)	125
Update time (s)	145
Elevation angle (°)	0.25, 1, 2, 3, 4, 5, 6.5, 9 (total 8)

Table IV 1 : Specifications and scanning details for OU-prime Radar

In this work, the storm of interest is located within the range of less than 60km, from OU-PRIME radar, with RHI scan from 0° at 20° elevation angle with prt of 0.8475ms. the azimuth scan is defined between 233° and 234°.

RHI and PPI scan: When scanning in PPI mode, the radar holds its elevation angle constant but varies its azimuth angle. The returns can then be mapped on a horizontal plane. If the radar rotates through 360 degrees, the scan is called a "surveillance scan". If the radar rotates through less than 360 degrees, the scan is called a "sector scan". And, when scanning in RHI mode, the radar holds its azimuth angle constant but varies its elevation angle. The returns can then be mapped on a vertical plane. The elevation angle normally is rotated from near the horizon to near the zenith (the point in the sky directly overhead). In this work we discuss only the results obtained by RHI scan.

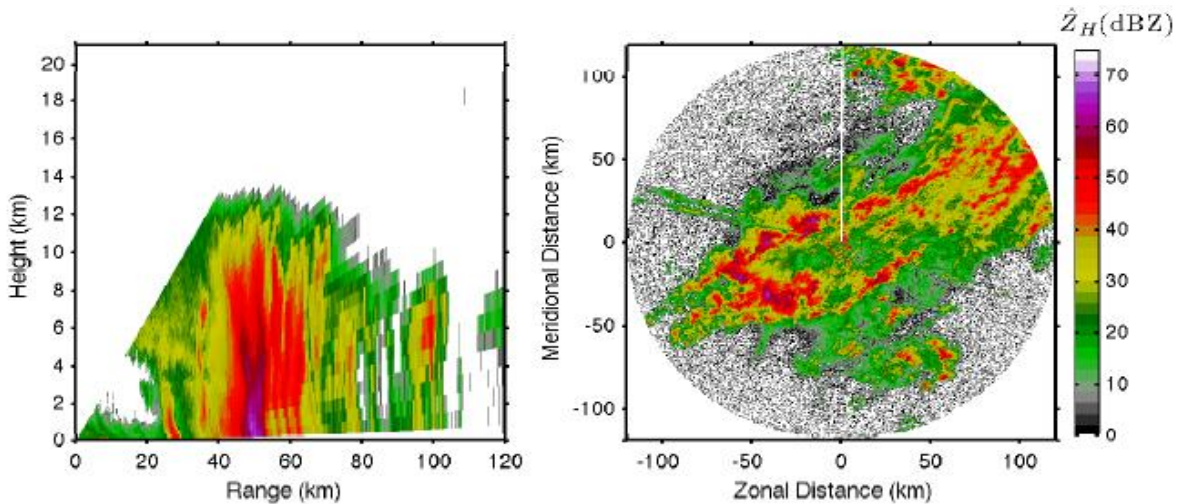


Figure IV 4 : RHI scan (left panel) and PPI scan (right panel)

IV.3.2 OU-PRIME data processing:

In this section, we discuss briefly the processing data of OU-PRIME:

For the IQ signal from each pulse, the azimuth and elevation angles are known. For example, the azimuth angle and elevation angles of OU-PRIME RHI pulses at 18:58:21 UTC 24 April 2011 are shown:

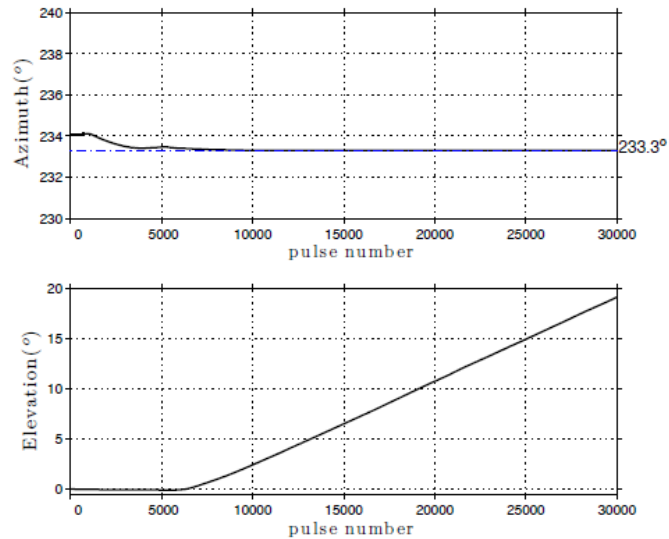


Figure IV 5 : Azimuth and elevation angle versus pulse number of the OU-PRIME's RHI scan at 18:58:21 UTC. (From Mosonet stations measurements)

We observe that a very large number of samples (approximately 6,500) were collected at elevation angle of approximately 0° and azimuth angle between 234° and 233° .

The complex signals IQ are stored and organized on a three dimensional matrix $V(A,G,M)$ where A: is the number of elevation angle ready for data processing, G: is the number of range gates, M: is The number of samples.

The first step is to select the number of samples for each radial, larger number of M must be selected to allow higher number of spectral averaging for improving statistical quality of the estimates of spectral polarimetric variables. (In this work a constant number of samples is selected ($M=960$) for each radial).

In this work, 39 elevation angles ($A=39$) are obtained from 0° to 19° with 0.5° interval (The 0.5° interval is selected based on the antenna beamwidth of OU-PRIME), the number of range gates ($G=960$) for each radial.

A noise power of 3.8 dB and 3.2 dB for H and V channels of \hat{Z} are used. Moreover, a calibration for \hat{Z}_{DR} of 0.1 dB is added (Palmer et al., 2011).

A flow chart for signal processing for base moments and polarimetric variables is shown in the figure VI.6:

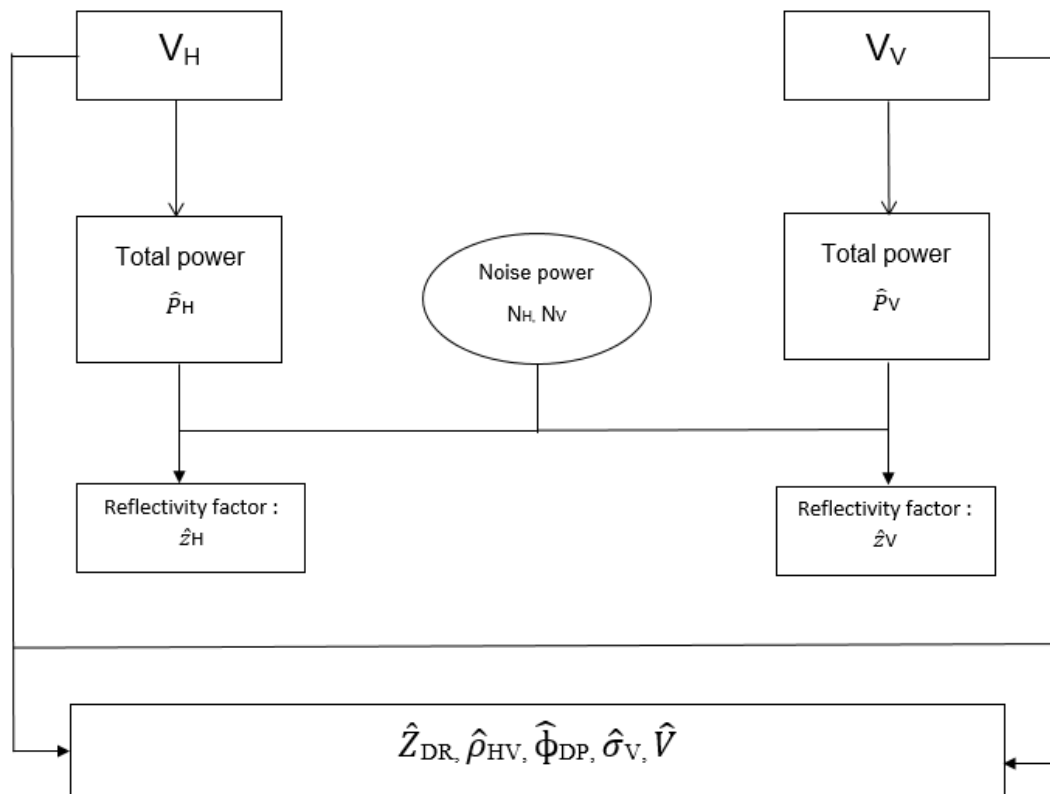


Figure IV 6: A flow chart for data processing to generate spectral moments and polarimetric variables.

After estimating the base DATA (base moments and polarimetric variables), Spectral polarimetric variables are calculated, the follow chart shown in the Figure (IV 7) describes the steps to estimate them.

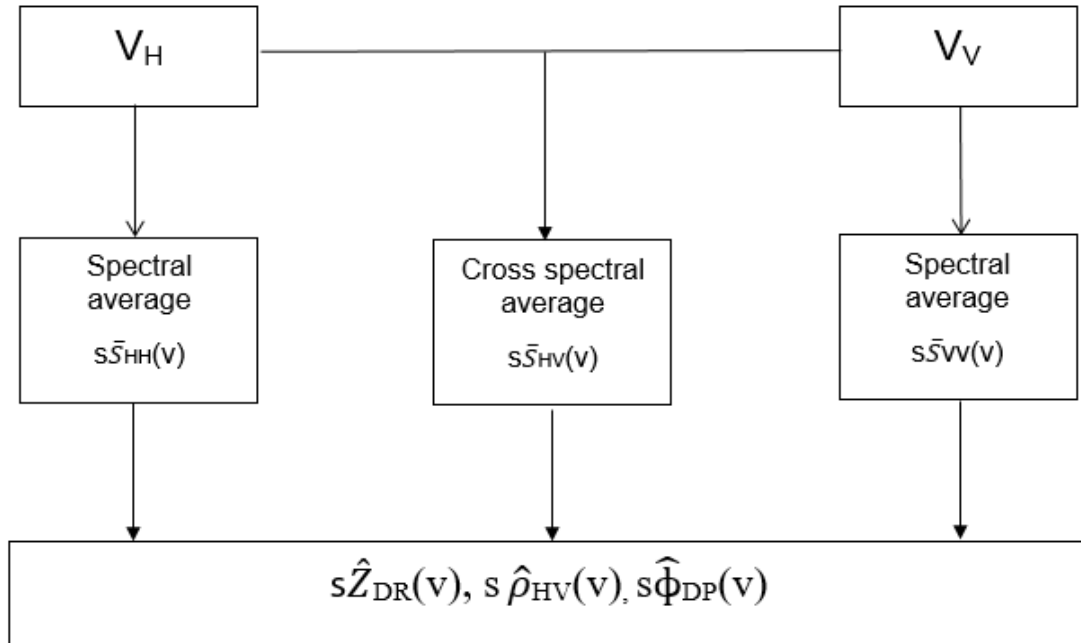


Figure IV 7: A flow chart for data processing on spectral polarimetric variables.

IV.3.3 Analysis and discussion:

Before discussing the results obtained, it is necessary to talk briefly about HCA (hydrometeor classification algorithm), The HCA discriminates between 10 classes of radar echo (as shown in the Figure IV 7) using six radar variables: the radar reflectivity factor at horizontal polarization Z_h , the differential reflectivity Z_{DR} , the cross-correlation coefficient ρ_{hv} between horizontally and vertically polarized radar returns, the specific differential phase K_{DP} , the standard derivation $SD(Z_h)$, and the standard derivation $SD(\phi_{DP})$ [40]

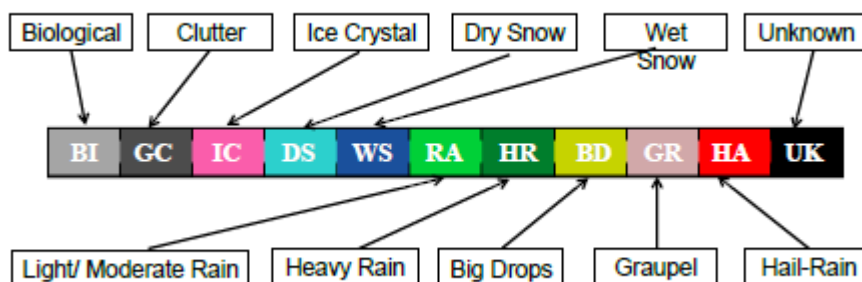


Figure IV 8: Classes HCA

The observation of hailstorm is shown in the Figure IV 9 \hat{Z}_h , \hat{Z}_{DR} , and $\hat{\rho}_{HV}$ from OU-PRIME's RHI scan at 18:58:21 UTC are shown in the left column, and $\hat{\sigma}_v$, \hat{V}_d , $\hat{\phi}_{DP}$ in the right column:

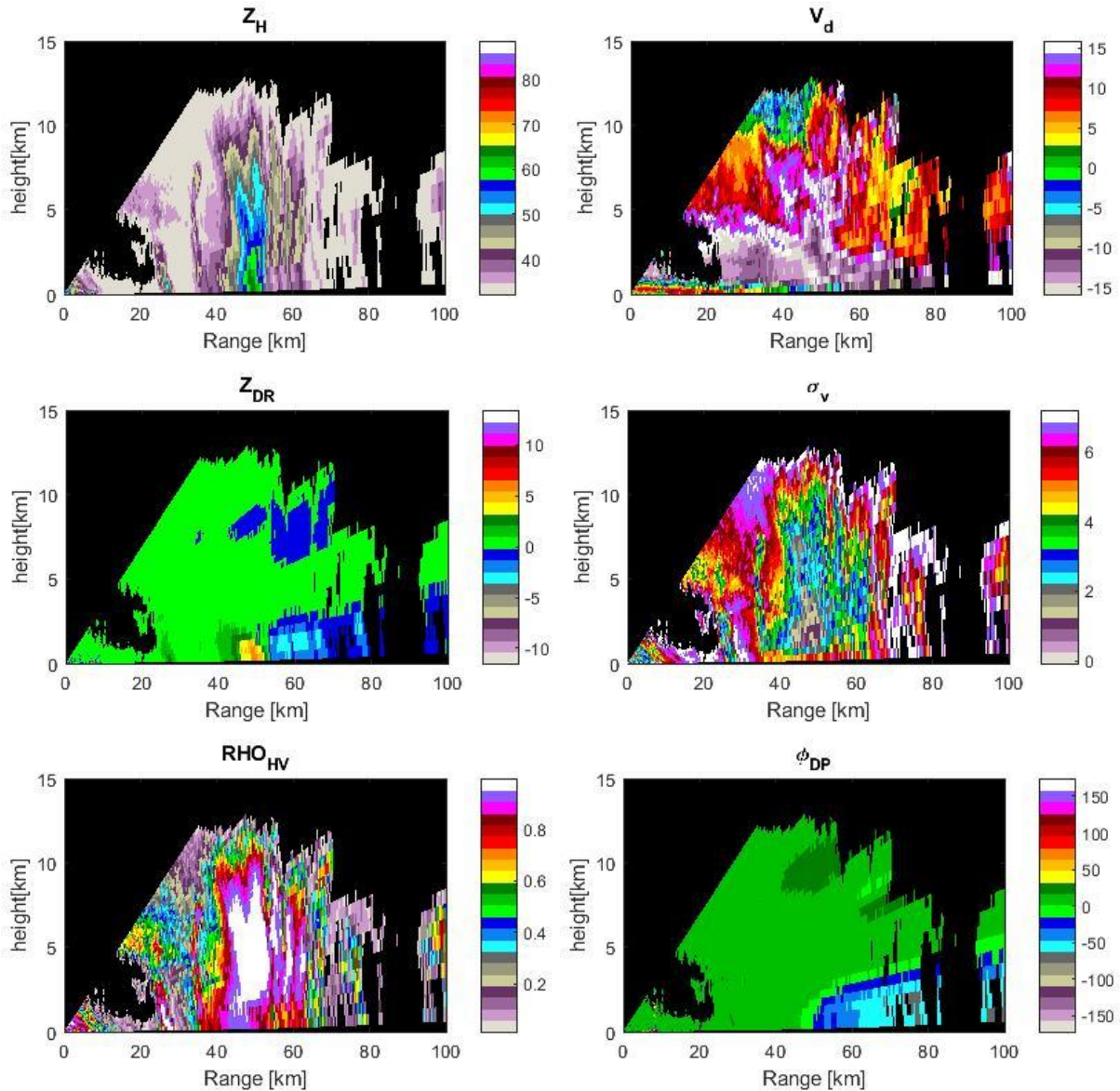


Figure IV 9: Reflectivity, differential reflectivity and co-polar correlation coefficient, radial velocity, spectrum width and differential phase (OU-PRIME RHI at 18:58:21 UTC)

The polarimetric variables Z_H , Z_{DR} , are the primary variables analyzed to characterize hail. Then ρ_{HV} is used to identify potential areas of Rain-hail mixture associated with melting hail.

Observations: the RHI scan shows:

- Area (1): an area of maximum value of Z_H ($Z_H > 65 \text{ dB}$) associated with a high value of Z_{DR} ($Z_{DR} > 4 \text{ dB}$) and low ρ_{HV} ($\rho_{HV} < 0.9$), at the range of 48-55 km from Radar near the surface.
- Area (2): an extensive region of low Z_{DR} ($Z_{DR} < 1$), is observed with high Z_H ($60 > Z_H > 45 \text{ dB}$) behind area (1).
- Area (3): At a high elevation angle, (i.e. height $> 5 \text{ KM}$, RANGE $> 48 \text{ km}$), RHI scan shows a low negative value of Z_{DR} ($0 \text{ dB} > Z_{DR} > -1 \text{ dB}$), associated with a high value of Z_H ($50 \text{ dB} > Z_H > 40 \text{ dB}$) and low ρ_{HV} ($\rho_{HV} < 0.9$).
- RHI scan of radial velocity Vd , and spectrum width, are early discussed.

Discussion:

Area (1): is evident that the high reflectivity region ($> 65 \text{ dB}$) has identified by the radar at the range of approximately 45 - 55 km from OU-PRIME at 18:50:29 UTC, which is consistent with hail report, this area is considered the core of storm.

The high value of Z_H is explained by the existence of a particles of large diameters possibly large raindrops, hail, and melting hail. According to Picca and Ryzhkov 2012 [41], and Meischner and Al. (1991) [43], enhanced Z_H and Z_{DR} , associated with low ρ_{HV} , in addition, attenuation of as low as -3 dB behind in this region (area 2), is caused by large drops mixed with melting hail.

Area (2): The low values of Z_{DR} ($0 < Z_{DR} < 1$) associated with the high value of Z_H is the classic signature of hail.

Area (3): The negative Z_{DR} with high value of Z_H at height $> 5 \text{ KM}$ (above freezing level, where the temperature is less than 20°F equivalent of -6.66°C) could be indicatives of falling dry hail [2], and very low value of ρ_{HV} is explained by a complex shape of giant dry hail.

In these three areas differential phase shifting $\hat{\Phi}_{DP}$ is near zero, which is attributed to the hail.

For radial velocity scan: negative values mean that the particles fall and positive values mean that the particles rise because of transient size sorting mechanism due to the dependence of The falling velocity of hydrometeor on its size.

The analysis of the observations suggests the presence of mixture of hail and rain at low elevation angle near at range of approximately 48 - 55 km at 18:58:21 UTC (in the core of hailstrom), and a giant dry falling hail at higher height. According to a National Oceanic and Atmospheric Administration storm report, hailstone of 1.9 cm was observed at 18:50 UTC at Rush Spring (approximately 50 km southwest of OU-PRIME), which proves the validity of this estimate.

However, signatures of hail need to be better understood in order to properly identify hail and estimate hail size, thus spectral polarimetry was applied.

Before moving to the spectral study, a quick look of radial velocity and spectrum width at (48 – 55km) is examined for investigating the kinematic proprieties of the hail region. The zoom of radial velocity and spectrum width RHI scan at 18:58 UTC are shown in the following figure:

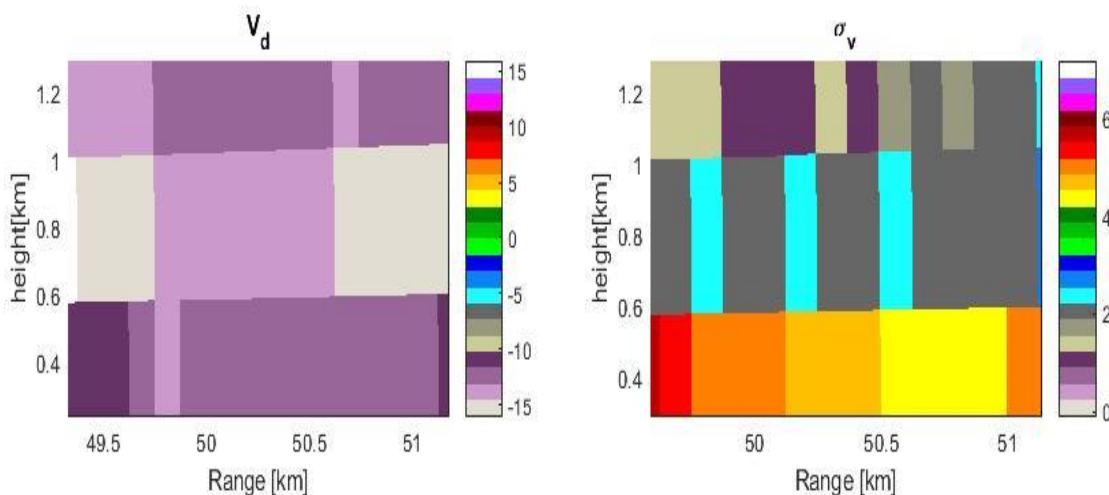


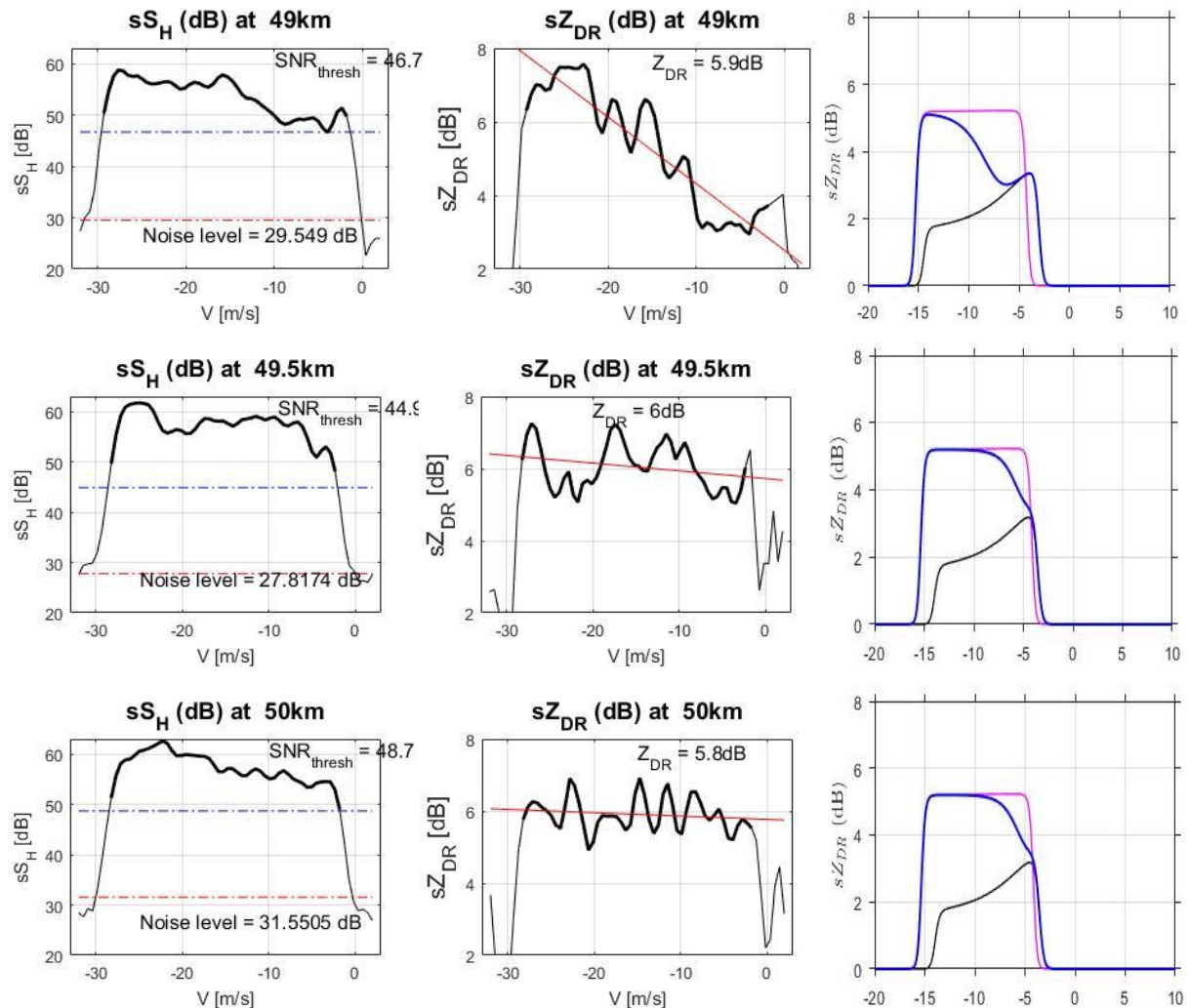
Figure IV 10: Zoom of radial velocity and spectrum width (OU-PRIME RHI at 18:58:21 UTC)

It's shown that spectrum width at the first elevation angle is relatively large ($4 - 5 \text{ ms}^{-1}$), which indicates a large dispersion of radial velocity. In addition, the mean radial velocity derived from radar is not constant (it varies between $[-10, -15 \text{ ms}^{-1}]$, these indicate the presence of strong turbulence and shear.

It can be concluded that this storm of interest had the presence of vertical shear, turbulence and existence of rain and hail at these ranges and lowest elevation angle of 0° .

IV.4 Application of spectral polarimetry to hailstorm:

In this work, on interest to hail signature in spectral reflectivity and differential reflectivity at ranges 49, 49.5, 50, 50.6 km at 0° elevation angle (50,50.6 KM are considered as within the core of the hail storm). In the figure 6.10 the spectral reflectivity \hat{S}_H , and differential reflectivity \hat{S}_{DR} , are shown at the selected ranges, additionally, the results of simulation applied in the precedent chapter, The thicker lines of \hat{S}_H , and \hat{S}_{DR} , are \hat{S}_H , and \hat{S}_{DR} above the SNR threshold (above the blue line) this is the only part of the spectrum used in this analysis. The spectral SNR threshold is determined based on the work of Yu et al. (2012) [28]. Additionally, \hat{Z}_{DR} values are also shown on the top of each \hat{S}_{DR} , subplot, and the slopes are denoted by red lines.



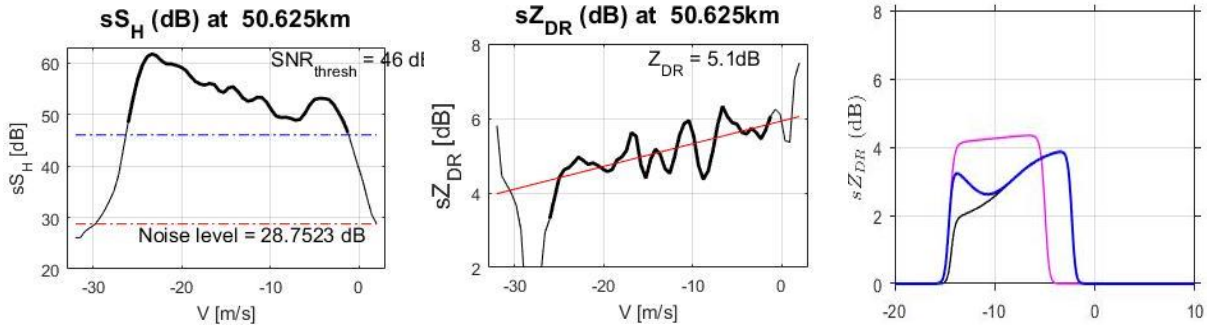


Figure IV 11 : Plots of the spectral reflectivity, differential spectral reflectivity at 49Km, 49.5Km, 50Km and 50.6Km and the simulation results.

It is clearly at 0° elevation angle, from all ranges, \hat{S}_H is broaden, $s\hat{Z}_{DR}$ have slopes that change with range, \hat{Z}_{DR} values are approximately between $4 - 6dB$ associated with high values of \hat{S}_H . According to the simulation applied in the precedent chapter, these different slopes are resulted from mixture of two different types of hydrometeor; $4 - 6dB$ of \hat{Z}_{DR} values are contributed to the mixture of rain and melting hail. Broad spectrum can be contributed from turbulence, broad and flat-top spectra in range 49.5-55 km are observed in strong shear environment. Therefore, these results confirm those that were obtained beforehand by the polarimetric variables RHI scan.

It is evident that the spectrum of $s\hat{Z}_{DR}$ at different ranges exhibits interesting and distinct variations which suggests the presence of size sorting of hydrometeors caused by vertical shear in a turbulent environment.

At the range 49km: $s\hat{Z}_{DR}$ spectrum has negative steep slope, $\hat{Z}_{DR} \approx 6.5 dB$ at $-27ms^{-1}$ is dominant by large raindrops. On the other hand, the lower value $s\hat{Z}_{DR}$ of approximately 4 dB at $0ms^{-1}$ is mainly contributed from hail.

At the range 49.5 and 50 km: high $s\hat{Z}_{DR}$ values with zero slope is observed from mixture of dominating large raindrops and fewer hailstones.

At the range 50.6km: $s\hat{Z}_{DR}$ spectrum has positive slope which is contributed from high amount of melting hail, and smaller amount of raindrops.

Conclusion:

Based on the previous results, we conclude that spectral processing provides more information about the environment.

General conclusion

General conclusion:

The main objective of this study is to explain the fundamentals of dual polarimetric radar and the estimation methods used to detect the different microphysical properties, kinematics and dynamics of a given precipitation system and then simulation was successfully conducted to deduce the limits of its estimates.

A natural phenomenon in precipitation systems called size sorting, marks important signatures on the results obtained by spectral polarimetry method. So, a simulation is implemented to analyze these signatures and interpret them in order to better estimate the properties of the precipitation system. The theory is subsequently applied to simulate Doppler and differential reflectivity spectra is derived, considering a mixture of rain and melting hails falling through a shear and turbulence environment.

A hailstorm on 24 April 2011 was observed by C-band OU-PRIME. Such dual-wavelength observations have been used to gain more information about the microphysical properties of hailstorm. The results obtained are compared with storm report from the National Oceanic and Atmospheric Administration. The OU-PRIME's RHI data at the lowest elevation angle (0°) were used to calculate spectral polarimetry, using simulation results previously applied, where the impacts of particle size distribution, shear, turbulence and mixture of rain and melting hail on polarimetric spectral signatures are investigated with the simulated Doppler spectra and spectral differential reflectivity. Finally, we have been able to obtain information on the different kinematic and dynamic microphysical properties of this hailstorm.

For future studies:

In this work, we focused on only one of the spectral polarimetric variables, spectral differential reflectivity, at the lowest elevation. Two other variables of spectral correlation coefficient and spectral differential phase can provide different aspects of microphysical properties. Moreover, the transition of spectral polarimetric variables from lower to high elevation angles can potentially help the understanding of the evolution of hailstorm.

In reality, microphysical processes such as evaporation, collision, coalescence, and break up cause rain DSDs to vary in size but were neglected for simplicity. This analysis only examined size sorting due to vertical shear of horizontal winds and neglected that due to transient effects updrafts and the storm-relative mean wind, a more realistic model can be used in the simulation to better explore the spectral polarimetric signature.

Future Weather Phased Array radar:

As with any new technology, significant challenges exist, such as combining radar polarimetry with phased array radar which has been used in military services for decades and is just now being tested in the weather radar community, is electronic beam scanning using phased array radar, which operates in a completely different way without any mechanical motion. To observe full 360-degree coverage, four phased array panels are needed. Each face azimuthally scans $\pm 45^\circ$ about a vertical plane, furthermore; the beam agility provided by electronic steering allows adaptive scanning so the beam needs only to scan stormy regions of interest rather than having equal dwell times on regions of clear skies. Because of this capability, phased array weather radars hold promise for improved observations of rapidly evolving severe weather phenomena.

Bibliography

- [1]: Gloria Kulesa; Weather and Aviation: How does weather affect the safety and operations of airports and Aviation and how does FAA work to manage weather-related effects?
- [2]: Doviak R. J. and D. S. Zrnić, 1993: Doppler Radar and Weather Observations. Academic Press, San Diego, California, 562 pp.
- [3]: Alexander V. Ryzhkov and D. S. Zrnić, 2019: Radar Polarimetry for Weather Observations. Springer Nature Switzerland AG, Switzerland, 486 pp.
- [4]: Zhang, Guifu, 2017, Weather radar polarimetry, CRC Press, Boca Raton, 304pp.
- [5]: Skolnik M. I., 2003: Introduction to radar systems. 2nd ed., McGraw-Hill. Education Pvt Limited.
- [6]: Hong Le, 2013, Thesis: Application of spectral polarimetry to a hailstorm at low elevation angle using c-band polarimetric radar, University of Oklahoma, Oklahoma, 157pp.
- [7]: Doviak R. J. al, 1979: Doppler Weather Radar, PROCEEDINGS OF THE IEEE, Vol. 67, N°11, pp 1522- 1553.
- [8]: Pruppacher, H. R. and R. L. Pitter, 1971: A semi-empirical determination of the shape of clouds and raindrops. J. Atmos. Sci., 28, 86-94.
- [9]: Gunn, R. and G. D. Kinzer, 1949: The terminal velocity of fall for water droplets in stagnant air. J. Meteor., 6, 243-248
- [10]: Beard & Prupacher 1969: A determination of the terminal velocity and drag of small water drops by means a a wind tunnel. J Atmos. Sci, 26,1066-1072.
- [11]: John H. van Boxel, J, 1998, Numerical model for the fall speed of raindrops in a rainfall simulator,
- [12]: Marshall, J. S. and W. Palmer, 1948: The distribution of raindrops with size. J.Meteor, 5, 165-166.

- [13]: Foote, G. B. and P. S. D. Toit, 1969: Terminal velocity of raindrops aloft. *J. Appl. Meteor.*, 8, 249-253.
- [14]: Yau, M.K.; Rogers, R.R. *A Short Course in Cloud Physics*; Elsevier: Amsterdam, The Netherlands, 1996.
- [15]: Ulbrich, C. W., 1983: Natural variations in the analytical form of the raindrop size distribution. *J. Climate Appl. Meteor.*, 22, 1764-1775.
- [16]: Saunders, M. J., 1971: Cross polarization at 18 and 30 GHz due to rain. *IEEE Trans. Antennas Propagat.*, AP19, 273-277.
- [17]: Brussaard, G., 1974: Rain-induced cross polarization and raindrop canting. *Elec. Letters*, 10, 411-412.
- [18]: Magono and Lee 1966: Meteorological classification of natural snow crystals. *Journal of the Faculty of Science, HOKKaido University* 7: 321-362.
- [19]: Pruppacher, H. R., and J. D. Klett, 1978: *Microphysics of Clouds and Precipitation*. Reidel, 954 pp.
- [20]: Bringi, V. N. and V. Chandrasekar, 2001: *Polarimetric Doppler Weather Radar Principles and Applications*. Cambridge University Press, Cambridge, UK, 636 pp.
- [21]: Mitchell, D. L., 1996: Use of mass- and area-dimensional power laws for determining precipitation particle terminal velocity. *J. Atmos. Sci.*, 53, 1710-1723.
- [22]: Spek, A. L. J., C. M. H. Unal, D. N. Moisseev, H. W. J. Russchenberg, V. Chandrasekar, and Y. Dufournet, 2008: New technique to categorize and retrieve the microphysical properties of ice particles above the melting layer using radar dualpolarization spectral analysis. *J. Atmos. Oceanic Technol.*, 25, 482-497.
- [23]: Aydin, K. and Y. Zhao, 1990: A computational study of polarimetric radar observables in hail. *IEEE Trans. Geosci. Remote Sens.*, 28 (4).
- [24]: Vivekanandan, J., R. Raghavan, and V. N. Bringi, 1993: Polarimetric radar modelling of polarimetric radar modeling of mixtures of precipitation particles. *IEEE Trans. Geosci. Remote Sens.*, 31 (5).

- [25]: Jung, Y., G. Zhang, and M. Xue, 2008a. Assimilation of simulated polarimetric radar data for a convective storm using the ensemble Kalman filter. Part I: Observation operators for reflectivity and polarimetric variables. *Monthly Weather Review*, 136, 2228–2245.
- [26]: Al-Khatib, H. Seliga, and V. N. Bringi, 1979: Differential reflectivity and its use in the radar measurement of rainfall. *Atmos. Sci. Prog. Ref.*
- [27]: Dual-Polarization Radar Operations Course: 2014. Presented by the Warning Decision Training Branch.
- [28]: Yu, T. Y., X. Xiao, and Y. Wang, 2012: Statistical quality of spectral polarimetric variables for weather radar. School of Electrical and Computer Engineering, University of Oklahoma.
- [29]: Zrnić .D. S, 1975: Simulation of weatherlike Doppler spectra and signals. *J. Appl. Meteor.*, 14, 619–620.
- [30]: Kumjian, M. R. and A. V. Ryzhkov, 2012: The impact of size sorting on the polarimetric radar variables. *J. Atmos. Sci.*, 69, 2042-2060.
- [31]: Gunn, R., and Marshall, 1955: The effect of wind shear on falling precipitation. *J. Meteor.*, 12, 339–349.
- [32]: Brussaard, G., 1976: A meteorological model for rain-included cross polarization. *IEEE Trans. Antennas Propagat.*, 24, 5-11.
- [33]: Bohne, A. R., 1982: Radar detection of turbulence in precipitation environments. *J. Atmos. Sci.*, 39, 1819-1837.
- [34]: Beard, K. V. and A. R. Jameson, 1983: Raindrop canting. *J. Atmos. Sci.*, 40 (448-453).
- [35]: Yanovsky, F. J., 2011: Inferring microstructure and turbulence properties in rain through observations and simulations of signal spectra measured with Doppler polarimetric radars, 501{542. *Polarimetric Detection, Characterization, and Remote Sensing*, NATO Science for Peace and Security Series C, Springer.

- [36]: Spek, A. L. J., and al 2008: New technique to categorize and retrieve the microphysical properties of ice particles above the melting layer using radar dualpolarization spectral analysis. *J. Atmos. Oceanic Technol.*, 25, 482-497.
- [37]: Wang, Y., 2010: The application of spectral analysis and artificial intelligence methods to weather radar. Ph.D. thesis, University of Oklahoma.
- [38]: Zhang, G., J. Viekanandan, and E. A. Brandes, 2001: A method for estimating rain rate and dropsize distribution from polarimetric radar measurements. *IEEE Trans. Geosci. Remote Sens.*, 39, 830-841.
- [39]: Moisseev D. N. and al, 2006: Dual-polarization spectral analysis for retrieval of effective raindrop shapes. *J. Atmos. Oceanic Technol.*, 23, 1682-1695.
- [40]: Ryzhkov A.V. and D. S. Zrnić al, 2008: The hydrometeor classification Algorithm for the polarimetric WSR-88: Discription and application to an MCS. *Weather and forecasting*, pp 730-748.
- [41]: Picca, J. and A. V. Ryzhkov, 2012: A dual-wavelength polarimetric analysis of the 16 May 2010 Oklahoma city extreme hailstorm. *Mon. Wea. Rev.*, 140, 1385-1403.
- [42]: Meischner, P. F., V. N. Bringi, D. Heimann, and H. Holler, 1991: A squall line in southern germany: kinematics and precipitation formation as deduced by advanced polarimetric and doppler radar measurements. *Mon. Wea. Rev.*, 119, 678-701.